UNIVERSITY OF CALIFORNIA
RIVERSIDE

Fabrication and Characterization of Organic Solar Cells

A Dissertation submitted in partial satisfaction
of the requirements for the degree of

Doctor of Philosophy

in

Electrical Engineering

by

Emre Yengel

December 2010

Dissertation Committee:
Dr. Cengiz S. Ozkan, Chairperson
Dr. Mihrimah Ozkan
Dr. Kambiz Vafai

The Dissertation of Emre Yengel is approved:

_____

_____

_____

Committee Chairperson

University of California, Riverside

To my wife

ABSTRACT OF THE DISSERTATION

Fabrication and Characterization of Organic Solar Cells

by

Emre Yengel

Doctor of Philosophy, Graduate Program in Electrical Engineering

University of California, Riverside, December 2010

Prof. Cengiz Ozkan, Chairperson

Bulk heterojunction organic solar cells have recently drawn tremendous attention because of their technological advantages for actualization of large-area and cost effective fabrication. Two important criteria of these cells are efficiency and cost. The research in this dissertation focuses on the enhancement of these criteria with two different approaches. In the first approach, power conversion efficiency of organic photovoltaic devices is enhanced by introducing Deoxyribonucleic acids DNA into the device structure. DNA provide exciting opportunities as templates in self assembled architectures and functionality in terms of optical and electronic properties. In the first method, we investigate the effects of DNA and metalized DNA sequences in polymer fullerene bulk-heterojunction (BHJ) solar cells. These effects are characterized via optical, quantum

efficiency and current-voltage measurements. We demonstrate that by placing on the hole collection side of the active layer, DNA and Pt-DNA sequences lead to an increase in the power conversion efficiency (PCE) by %16 and %30, respectively. Furthermore, we studied the electrical charge characteristics of our DNA layer by using capacitance-voltage (C-V) measurements to explain the increase in hole collection which shows that spray coated DNA formed a negative layer which can increase the hole collection in the cathode side. In the second approach, device cost is tried to reduce by replacing the most expansive material, indium thin oxide (ITO) thin films, with graphene thin films. Large area graphene films were grown with chemical vapor deposition (CVD) method. It is observed that, its pristine form, the electrical and surface properties of these films are not sufficient enough for the organic photovoltaic applications. These properties are enhanced with a surface treatment of Argon (Ar) plasma and nitric acid bath. The results of these treatments show that the surface becomes hydrophilic and surface resistance can be decreased by %25. Then, it is demonstrated that the PCE of the graphene based solar cells can be reached up to one tenth of the ITO based devices. The research conducted in this dissertation offers promising potential of bulk heterojunction organic solar cells as a clean and affordable source of energy source in the near future.

Table of Contents

List of Figures

List of Tables

Chapter 1:

Introduction

1.1 Renewable Energy Sources

The world's energy consumption rate has been skyrocketing continually since the industrialization era. As demand for energy keeps increasing, corresponding to the raising of world's population, we become more and more dependence on the limited amount of fossil energy, inherited from the Dinosaur era. (Figure 1.1)

In 2008, the level of energy consumption on the planet was approximately 15 terawatts (TW) [1]. Today, fossil energy provides %86.5 of the worldwide energy consumption. Based on the ongoing trend of the increase in the energy consumption over the years, it is reported that the anticipated level of energy consumption in 2050 will be 28–35 TW with an annual increase of %2 [2]. But, it's an evadable fact that limited reserves of fossil fuel will not be sufficient enough to supply this high demand. According to recent predictions, the inevitable permanent decline in the global oil production rate is expected to start within the next 10-20 years [3]. Moreover, as being the outcome of the energy derived from fossil fuels, carbon dioxide causes global warming as a result of our excessive abuse of the energy derived from fossil sources.

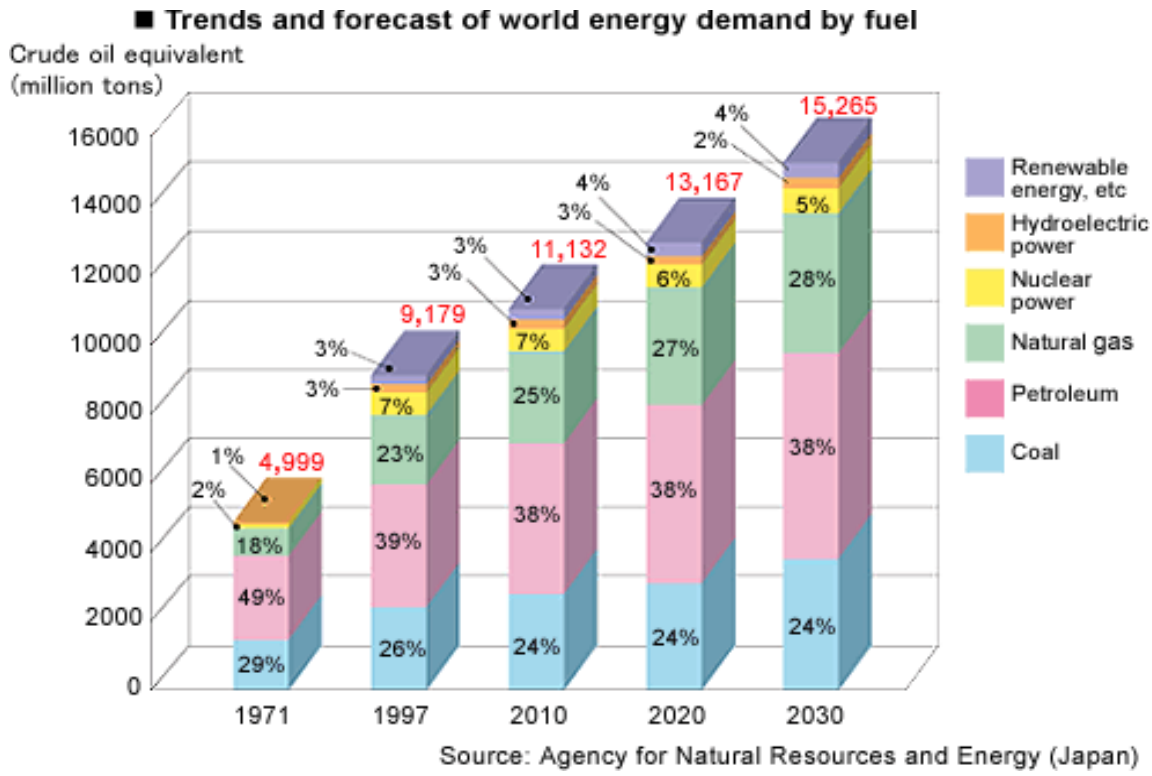

Figure 1-1 Past, recent and expected future energy usage of world in crude oil equivalents between 1971 and 2030 [4]

In this sense, renewable energy sources turn out a promising solution. Today, the renewable energy sources available are largely covered by hydropower, biomass energy, solar energy, wind energy, geothermal energy, and ocean energy. But it's evident that all these potential sources have some drawbacks; like geographical limitations, sustainability or environmental problems.

1.2 Solar Energy

As being the largest among carbon-neutral energy source, energy of sun gets a lot of attention in the last century. The energy capacity of the sun is examined in a report that the earth receives more energy from sun in one hour than it is using in one year [5]. It is estimated that sun has an available renewable energy of 86000 TW per year while earths' consumption is 15 TW per year. According to these values, even the projected energy consumption is doubled in the next 50 years, the sun has plenty of energy available. Therefore, solar energy harvesting can be a good candidate to the energy problem.

There are obvious logistical problems associated with solar energy. One of the main drawbacks of this energy is the storage of it. The energy we convert into electricity is lost if it is not used as it is generated. Wind, wave, and photovoltaic solar energy all suffer from the problem of not being energy technologies that inherently allow for storage while some technologies are suitable for storage, such as; nuclear power, hydropower, biomass, and geothermal power.

1.3 History of Solar Cells

The idea of converting solar energy into direct electrical power was first applied in semiconductor impurities at Bell laboratory in 1954 [6]. The initial power conversion efficiency of this first modern solar cell was 6%. After this milestone, solar cell research developed three generations of solar cells.

1.3.1 Inorganic Solar Cells

The first generation of solar cells, based upon silicon based P-N junction cells. These solar cells use a single junction of extremely pure silicon for extracting energy from photons, and have a theoretical efficiency maximum of 33% [7].

In the early 1960s, silicon based solar cells have ~11% efficiency. They were relatively inexpensive, and suitable for the low power and limited lifetime application [8]. The conversion efficiency of standard silicon solar cells ranges around 15% under standard test conditions.

In the last 50 years, there have been many enhancements in the silicon cell technology to improve their efficiency. During this time, research is mainly focused on better light absorption, extremely thin cells with back-surface reflectors for internal light trapping, and passivated cell surfaces to reduce losses due to recombination effects. The highest measured efficiency for a large-area (i.e., 5 in.2) crystalline silicon solar cell stands at 25%. (Figure1-2)

Although the manufacturing processes of these generation cells are very expensive, they still dominate the solar cell market. In 2007, first generation solar cells accounted for 89.6% of commercial production. It is not thought that first generation cells will be able to provide energy more cost effective than fossil fuel sources.

The high cost of the first generation cells give rise to the development of the second generation solar cells. This so called ‘thin film’ solar cell technology was first made by Wolf and Spitzer in mid 1980s [9]. This generation of solar cells has been developed based

on materials of crystalline silicon, micromorphous silicon [10], copper indium gallium selenide [11], and cadmium telluride [12]. They are significantly cheaper to produce than first generation cells but have lower efficiencies. In 2007, thin-film silicon production represented 5.2% of total market share. In 2010, copper indium gallium selenide based cells has the highest reported efficiency with is 20%. (Figure 1-2)

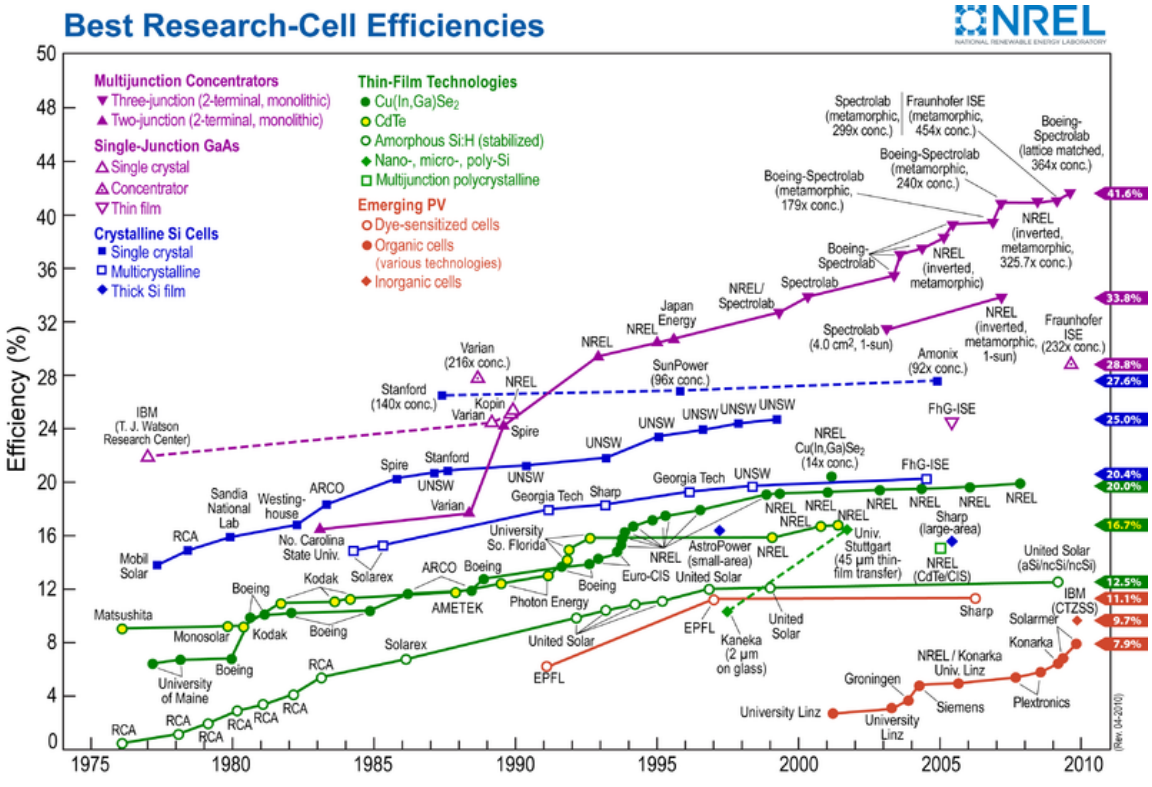

Figure 1-2 Best Research Cell Efficiencies in 2010, NREL [13]

1.3.2. Organic Solar Cells

After the discoveries of new organic photovoltaic materials, a third generation of photovoltaic devices based on organic solar cells became a very hot topic for scientists for

the last decade. These so called ‘plastic cells’ became a very promising solution to the upcoming energy problem because of their flexible structures, low fabrication costs, ease of processing and adjustable electrical properties.

Still in research phase, third generation cells has moved beyond silicon-based cells by using the evaluation of materials innovation technology. Targeted conversion efficiency for this organic material based generation is 30-60%. Although many scientists came up with different materials and structures to this energy harvesting problem using organic solar cells, the efficiencies of these devices are still not good enough for commercialization. It is recently reported that efficiencies of these devices have increased to 4-5% [14, 15]. Increasing the performance of these plastic cells is dependent on understanding and suppressing the effects of the performance limitations.

When considering the performance limitations, solar radiation should be investigated carefully. While this radiation covers the total electromagnetic spectrum, almost half of the energy exists in the short-wave (visible) part and one third of the energy lies in the infrared portions. So, during the last decade, research on the light harvesting started from the visible range and expanded to the entire spectrum. (Figure 1-3)

Generally, organic solar cells do not need the p-n junction necessary in traditional semiconductor. In the last 20 years, different organic materials, blends and structures are investigated to achieve highest efficiencies. Outcomes of these researches are organic solar cells, tandem solar cells, hybrid solar cells and dye-sensitized solar cells.

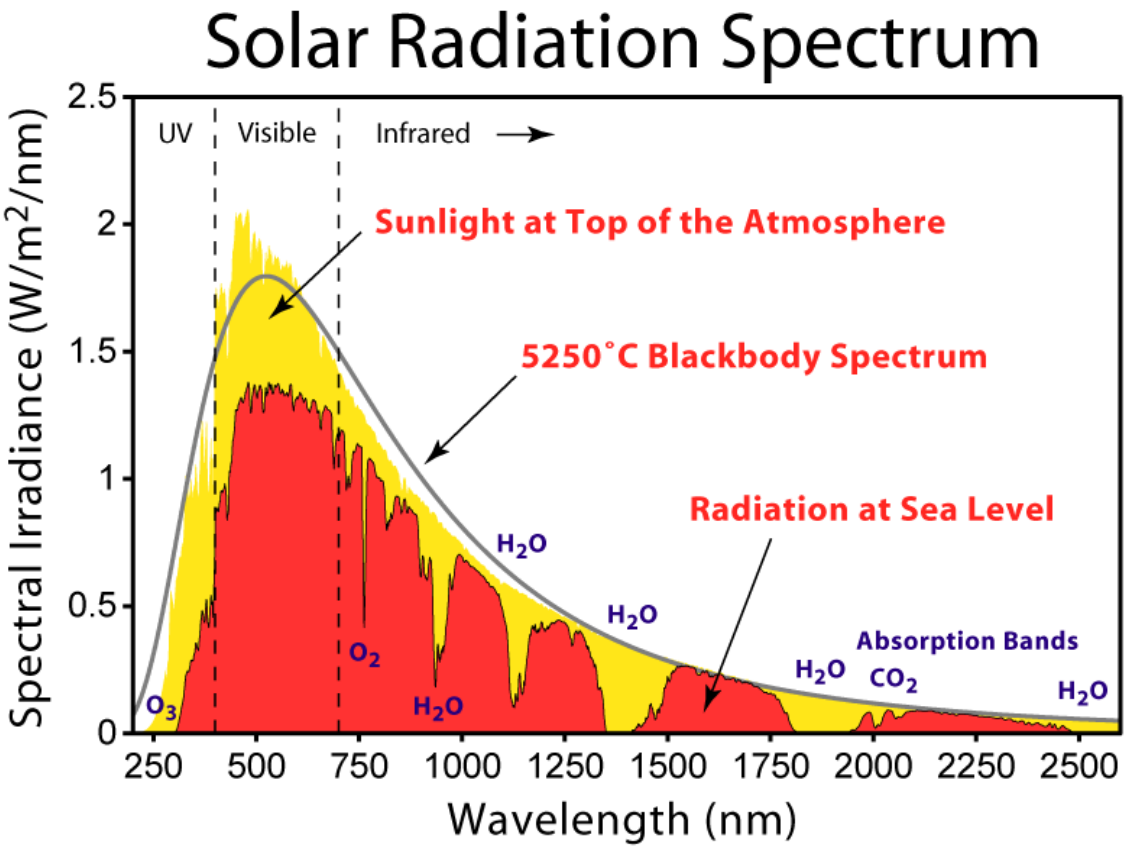

Figure 1-3 The Solar Spectrum at the Top of the Atmosphere and the radiation at Sea Level [16]

Chapter 2:

Basics of Organic Solar Cell

2.1 Organic Semiconductor Materials

The organic solar cell field started with the small organic molecules (pigments), but real breakthrough was achieved after the development of semiconducting polymers. Incorporating these conjugated polymers into organic solar cells resulted in remarkable improvements within the past years.

The milestone in the polymer solar cell was in 1977. In that year, Shirakawa, MacDiarmid, and Heeger demonstrated the conductivity of conjugated polymers can be controlled by doping. For this discovery, they were honored with the Nobel prize in chemistry in 2000 [17]. Since then, these conjugated polymers have been used successfully in LEDs [18-20] and solar cells [20, 21].

What makes these conjugated polymers attractive for solar cells is the bond structure between the carbon atoms. Different from most of the industrial plastics where the insulating properties of them come from the formation of σ bonds between the neighboring carbon atoms, in conjugated polymers these σ bonds forming the backbone are alternatingly single or double (Figure 2.1 left). In other words, in the backbone of the polymer, each carbon atom can only bind to only three of its four neighboring atoms which means that one electron per each carbon atom is left in the p_z orbital. Since this is the case for all the carbon atoms in the backbone, these unbounded electrons mutually overlap between these p_z orbitals, so that they form the π bonds along the backbone. So that, the

electrons on the π bonds can be delocalizing along this conjugated path to make the conjugated polymer an intrinsic semiconductor [22]. If the π band is filled with electrons, the band is called the highest occupied molecular orbital (HOMO), otherwise called as the lowest unoccupied molecular orbital (LUMO). If you excite the electrons in this π band, the polymer chain stays together without falling apart because of the σ bonds formed between the neighboring carbon atoms.

In conjugated systems, pi bonds (π bonds) are covalent chemical bonds, where two lobes of one involved electron orbital overlap two lobes of the other involved electron orbital. Only one of the orbital's nodal planes passes through both of the involved nuclei. Also, as the band gap of a conjugated system depends on its size,[22] The local HOMO and LUMO positions can be changed by changing the conjugation along the polymer's backbone. Therefore, real conjugated polymers are subject to energetic disorder.

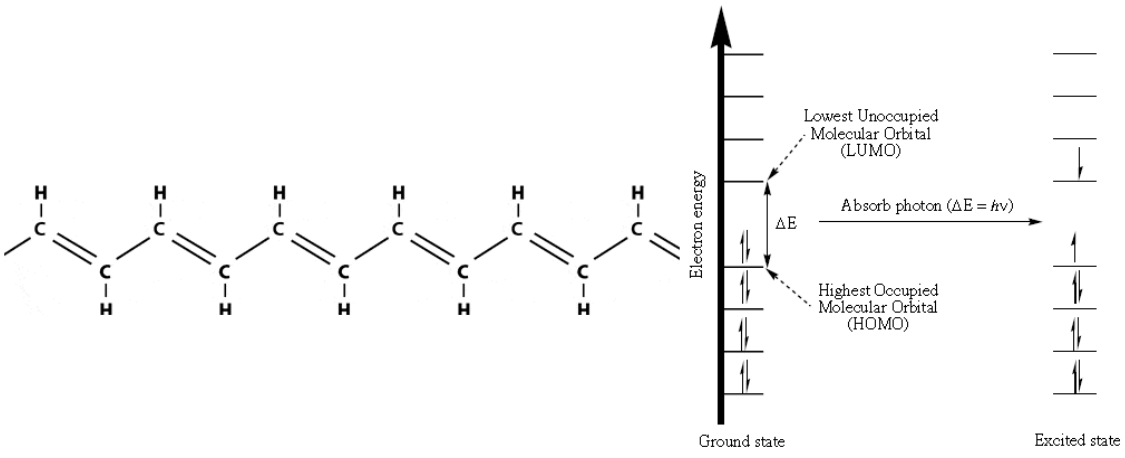

Figure 2-1 (left) In polyacetylene, the bonds between adjacent carbon atoms are alternatingly single or double [23] (right) Changes in the electron energy levels of a conjugated polymer before and after the photon absorption [24]

Hence, one way to move an electron from the HOMO level to the LUMO level by light absorption, if the energy of the absorbed photon is equal or greater than the energy of the orbital gap (band gap). Following the absorption of a photon with sufficient energy by the organic semiconductor, an electron moves into the LUMO, leaving a hole behind in the HOMO (Figure 2.1 right). However, after the separation, this electron-hole pair cannot be isolated due to electrostatic interactions but forms a tightly bound state called as exciton. The exciton binding energy for organic semiconductors (in a range of 200–500 meV) is one order of magnitude larger than inorganic semiconductors like silicon, where photo excitations lead direct free carriers at room temperature [25].

After the neutral-charge excitons generated via light absorption, they start to transport through diffusion. The diffusion length of an exciton is an important characteristic property of the conjugated polymers for optoelectronic applications that varies from 5nm to 20nm. However, the increase in the diffusion length decreases the exciton lifetime meaning that they either decay or dissociate through the internal mechanism. Therefore, the thickness of the conjugated polymer systems is restricted by the exciton diffusion length.

This diffusion mechanism is followed by dissociation for the excitons that are close enough to the layer interface. Then, electrons transfer into the acceptor at the donor-acceptor interface remaining the hole behind. The rest of the excitons decays through recombination. Therefore, the energy efficiencies of single-layer polymer devices remain typically below 0.1%.[25]

Then, dissociation of the electron-hole pair is transferred into the related electrodes. Efficiency of this process is related to different parameters. Some of which are the exciton diffusion length, carrier drift length and exciton lifetime.

In addition, the absorption bands of the materials used have a high impact on the overall efficiency. The absorption band of most conjugated polymer lies in a relatively narrow range of solar spectrum, as they are commonly known as intrinsic wide band gap semiconductors (band gap above 1.4eV).

The thermal energy at room temperature (~25 meV) is not sufficient to efficiently generate free charge carriers in organic materials by exciton dissociation, even at typical internal electric fields ($\sim 10^6$–10^7 V/m) [25], it is not an easy process. In many conjugated polymers most of the excitons cannot dissociate into free carriers in a pure layer [20].

2.2 Heterojunction Organic Solar Cell Architecture

While high recombination rates and low efficiencies in one layer organic solar cells made them inappropriate candidates for the future applications, the discovery of heterojunction organic solar cells opened a new era for this type of cells. According to this approach, polymer layer is made by hole and electron accepting organic materials and photo generated excitons in this layer dissociated into free carriers at the interface. Comparing with the single component solar cells, recombination rate of heterojunction solar cells is low. The charges are separated at the donor and acceptor molecule interface, caused by a large potential drop. When potential difference $\Delta\Phi$, the difference between the

ionization potential of the donor and the electron affinity of the acceptor exceeds the exciton binding energy, is achieved, excited electron charge is transfered from the higher LUMO level to the lower LUMO level. In other words, electron moves from the donor to the acceptor [25]. (Figure 2-2 right)

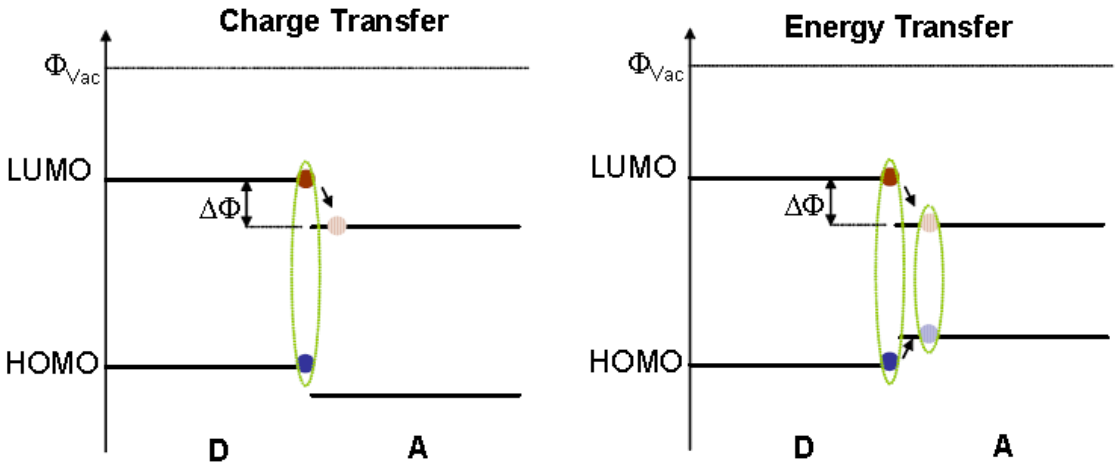

Figure 2-2 The interface between two different semiconducting polymers (D = donor, A = acceptor) can facilitate either charge transfer by splitting the exciton or energy transfer, where the whole exciton is transferred from the donor to the acceptor [25]

The efficiency of this exciton dissociation process, called as photo induced charge transfer, depends on some conditions. First of all, during the process, free charges can be generated only if the hole remains on the donor side of the interface which is due to the higher HOMO level of the donor. If the HOMO of the acceptor is higher, both electron and hole can be transferred to the acceptor side which leads to an energy loss. (Figure 2-2 left) The materials in the heterojunction layer should have an appropriate band gap to avoid this kind of an energy loss.

The thickness of this layer is also an important parameter for efficient exciton generation. This thickness should be higher that the exciton diffusion length to collect all the excitons that are able to diffuse to the interface. Also, the thickness of the heterojunction layer should be low enough to let the incident light penetrate efficiently through the layer. Therefore, the thickness of the active layer should be around 50-200nm.

2.2.1 Bilayer Organic Solar Cells

There are two main types of heterojunction solar cells. The most straightforward, also called as bilayer heterojunction, can be prepared by spin coating two different layers of polymers by one on the other (Figure 2-3a). Similar to the inorganic solar cell structures, directional photoinduced charge transfer across the interface is secured in this geometry of this type. After the exciton dissociation, both types of charge carriers travel in different layers. So, the chance for recombination is significantly reduced. The limiting factor on this type of heterojunction cells is the short length of the interfacial area.

2.2.2 Bulk Heterojunction Organic Solar Cells

A new structure based on the mixture of the electron donor and acceptor material is prepared to increase the interfacial area length and thus to improve exciton dissociation efficiency. This mixture of materials spin coated on the surface to form a heterojunction layer, also called as bulk heterojunction (Figure 2-3).

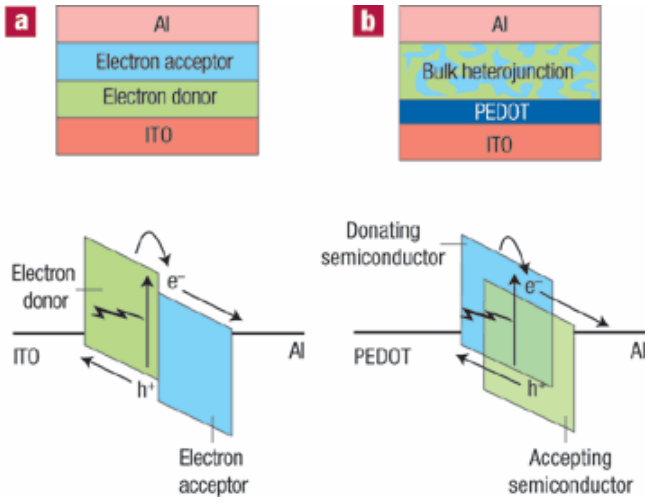

Figure 2-3 Different heterojunction solar cell structures and corresponding band diagrams [26]

In the literature, different types of heterojunction cells are considered by using different polymer blends and molecules. The list of some breakthrough materials and devices are shown in Table 2-1.

Table 2-1 Summary of device characteristics for various solar cell devices fabricated with different organic materials

System	Year	Fill Factor [%]	Efficiency white light [%]	Reference
PPV/C60	1995	-	-	[21]
POPT/CN-PPV	1998	35	1.9	[27]
MDMO-PPV/ [60]PCBM	2001	51	3.0	[28, 29]
P3HT/ PCBM	2002	55	4.9	[29, 30]
PTB7/$PC_{71}BM$	2010	69	7.4	[31]

Among different polymers, the buckminster fullerene C_{60} drew a lot of attention because of its' strong electron acceptor properties. It's based on experiments in bulk heterojunction cells that when C_{60} is mixed with hole conducting materials, photoconductivity increases under illumination [32]. But, C_{60} shows a tendency to crystallize in the polymer mixture. This leads to the development of PCBM, a derivative of C_{60} (Figure 2-4). By forming smaller crystallic structures in the blend, the solubility of PCBM increses.

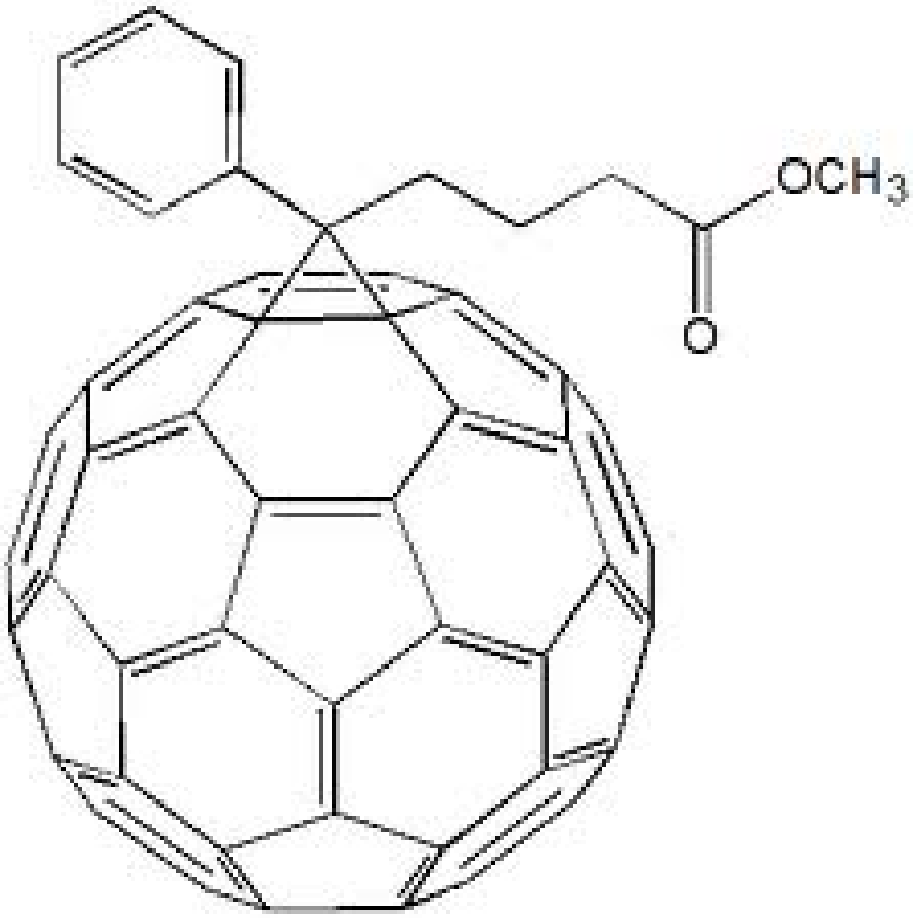

Figure 2-4 Electron-conducting acceptor polymer, a soluble derivative of C60, namely PCBM (1-(3-methoxycarbonyl) propyl-1-phenyl[6,6]C61) [33]

For the electron donor material, PPV derivatives were widely used until the development of P3HT (poly-3- hexylthiophene) (Figure 2-5). Being able to absorb photons at higher wavelengths than the PPV derivatives makes P3HT a more suitable partner for PCBM in organic solar cells. Studies on this pair showed that charge mobilities can be increased by slow drying of this layer during the fabrication. Therefore, charges can be collected more effectively forming the space charge region smaller.

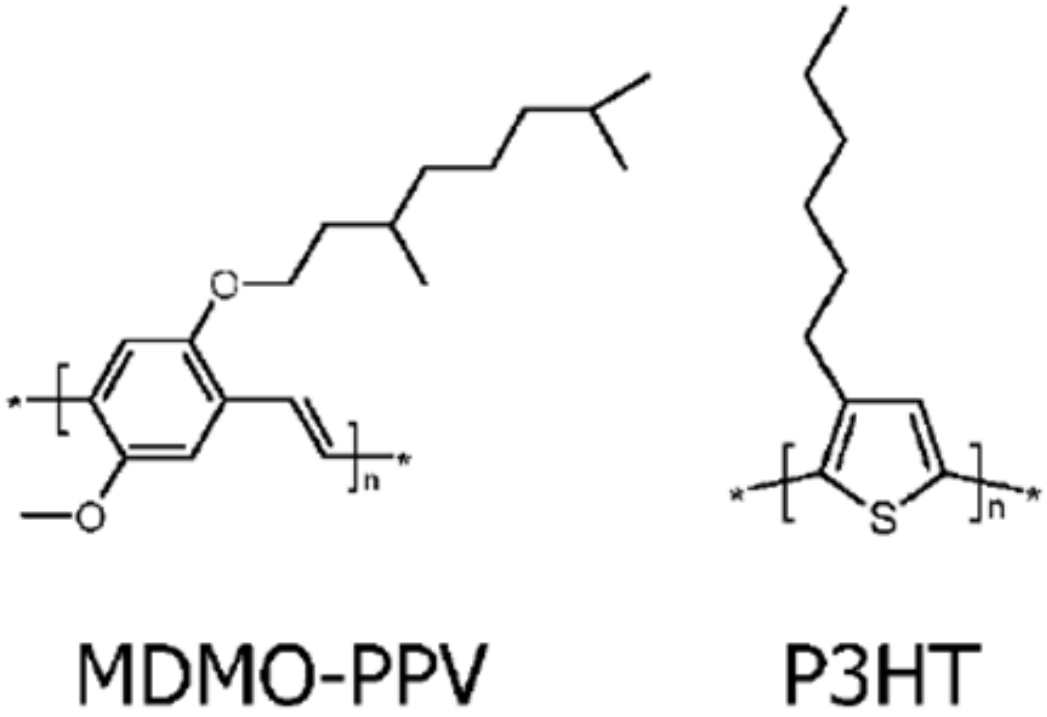

Figure 2-5 Some commonly used conjugated polymers are shown .Two important representatives of hole-conducting donor type polymers are MDMO-PPV (poly[2-methoxy-5- (3,7-dimethyloctyloxy)]-1,4-phenylenevinylene), P3HT (poly(3-hexylthiophene-2,5-diyl) [34]

2.2.3 Effect of the buffer layer and the electrodes in Organic Solar Cells

One of the early problems in bulk heterojunction organic solar cells is the possible short circuits between electrodes based on the fabrication of the thin polymer layer. These short circuits can cause from the gaps in the layers or from the morphology.

This problem is solved by spin casting another polymer layer between the anode contact ant the active polymer layer. Most common buffer polymer is poly-(3,4-ethylenedioxythiophene):poly-(styrenesulphonic acid) (PEDOT:PSS). Along with acting as an electron blocking layer, a thin semiconductor PEDOT:PSS layer works to prevent electron leakage from the bulk heterojunction acceptor to the anode, to help extracting the photogenerated holes and to planarize the contact surface.

Electrode materials have also important effect over the performance of organic solar cells. The work function of the electrode materials determines whether the electrode forms an ohmic or a blocking contact for the respective charge carrier. Moreover the difference in work function of the electrode materials has a considerable effect over the open circuit voltage. Common electrode materials for the electron collecting contact are Al (4.28eV), Ca(2.87), In(4.12eV) and Ag(4.26) (Figure 2-6).

Although some metals are used for the hole collecting side, it is not possible to form an high transparent metal electrode with low sheet resistance. For this reason so called conducting glasses are often used.

The most common electrode is Indium Tin Oxide (ITO) which is a degenerated semiconductor comprising a mixture of In_2O_3 (90%) and SnO_2 (10%) with a bandgap of

3.7eV. The large bandgap allows no absorption of wavelengths longer than about 350nm. The material can be highly conducting leading to very low sheet resistances for 100nm thick layers of ITO. When there is lack of oxygen, it acts as n- type dopant which is suitable for the anode contact applications.

As the thickness of the ITO layer increases, the sheet resistance decreases. Commercial available ITO coated glasses have a sheet resistance between 5-15 Ωsq^{-1} with a thickness of 100-150 nm. The transmission properties of the thicker ITO substrates do not change much since the material does not absorb in the visible. Nominal transmission is greater than 85% for the 150 nm thick substrates.

By this property, conjugated polymers with absorption in the whole visible range can be used with ITO if the bandgap of the polymer and the work function of the ITO can allow for the charges to move in the right direction. In this sense, ITO and PEDOT:PSS are suitable for the hole collection side of the organic solar cell devices. The energy diagram of an example solar cell is in figure with different cathode electrodes.

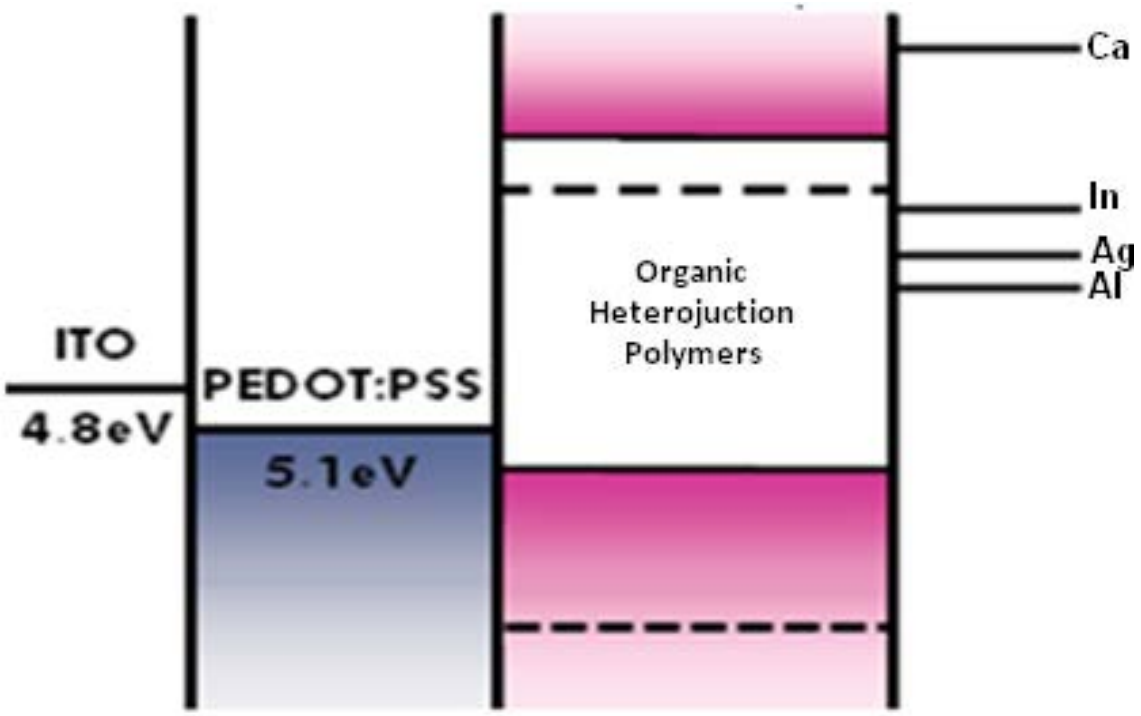

Figure 2-6 Energy diagram model of an bulk heterojunction organic solar cell with different cathode electrodes (Adapted from [35])

2.3 Solar Cell Characterization Parameters

2.3.1 Absorption Measurements

The first step in the collection of the charge carriers in the organic photovoltaic cells is the absorption of the incident light. The incident light generates electron–hole pairs at the *p*-type donor material due to exciting electrons from HOMO to LUMO bands. The absorption of these incident photons is measured by monitoring the reflection of the light by the organic solar cell. By using the fact that the addition of the reflection and the absorption is unity, absorption is calculated accordingly.

During the calculation of reflection, two reference spectrums are calculated; the white reference spectrum and the dark reference spectrum. Here, the white reference spectrum, R_{white}, is measured with a glass substrate having only a reflecting electrode. The dark reference spectrum, R_{dark}, is taken without any sample to compensate the internal reflections in the setup. After this reflection is calculated, the reflected signal R_{sample} is measured and decomposed in a spectrometer. Then, the reflectivity R and absorption A are calculated as [36];

$$A = 1 - R = \frac{R_{sample} - R_{dark}}{R_{white} - R_{dark}} \tag{2.1}$$

In the solar cell structure, photon absorption depends on the thickness of the donor material. Because the thickness of the donor material layer is of the same order of magnitude as the wavelength of the incident light, small changes in this layer thickness can have a significant effect on the absorption of the organic solar cell. So, absorption is one of the main limiting factors of the active layer thickness.

In the past, the optical thickness range for different organic films is studied by different groups [37, 38]. One example of these studies can be found in Figure 2.7.

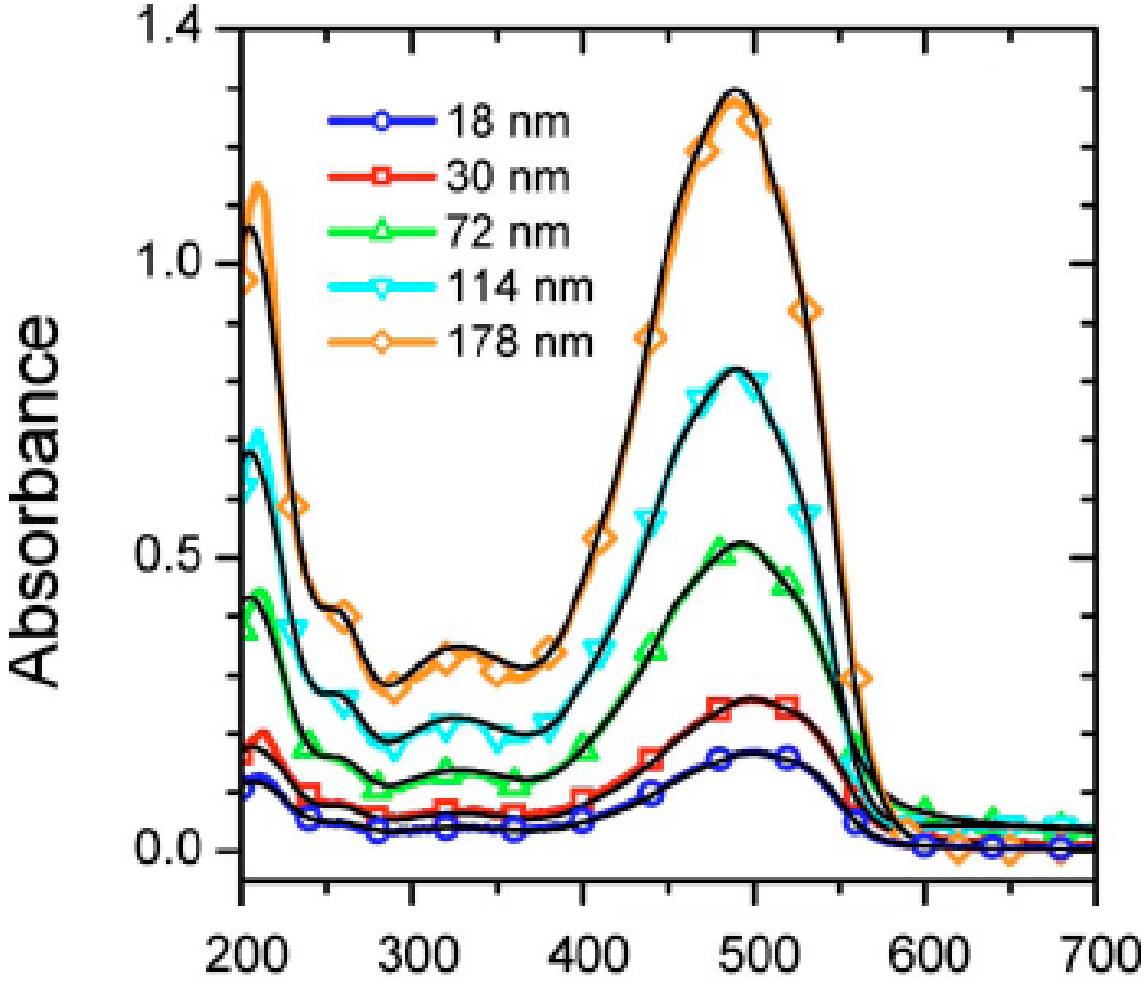

Figure 2-7 Absorption spectra measured for five films of MEH-PPV of different thicknesses [37]

2.3.2 Spectral Responsivity Measurements

Spectral responsivity measurements of organic solar cells are used to calculate the spectral mismatch correction factor and understand physical mechanisms of devices. This correction factor between the reference and test cells is used to set the light intensity of the solar simulator for solar performance measurements. The spectral responsivity, $S(\lambda)$, is calculated by [39];

$$S(\lambda) = \frac{q\lambda}{hc} QE(\lambda) \tag{2.2}$$

where the constant term q/hc equals 8.0655×10^5 for w in units of meters, $S(\lambda)$ in units of AW^{-1} and the quantum efficiency, QE(λ) in units of %.

Here, quantum efficiency (QE) or incident photon to converted electron efficiency (IPCE) describes the overall efficiency of the working mechanism of the bulk heterojunction solar cells. IPCE determines by the ratio of the photons that generate electrons in the external circuit to incident photons of monochromatic light per time and area [40];

$$IPCE = \frac{Number\ of\ extracted\ electrons\ (Ne)}{Number\ of\ incident\ photons\ (Np)} \tag{2.3}$$

One important parameter during the measurements of the spectral response of the organic solar cells is the response time of the cell to the chopped light. For polymer solar cells, the response of the device to the incident light is very fast. For a P3HT:PCBM device, the response time is less than a millisecond [39].

Another important parameter is the internal quantum efficiency. The IQE is the ratio of the number of charge carriers collected by the solar cell to the number of photons of a given energy that shine on the solar cell from outside and are not reflected back by the

cell, nor penetrate through (absorbed photons). If the optical losses in a solar cell are known, the IQE can be calculated as [40];

$$IQE = \frac{Number\ of\ extracted\ electrons\ (Ne)}{Number\ of\ absorbed\ photons\ (Np)} \tag{2.4}$$

The IQE only considers photons, which are absorbed in the active layer. It is therefore the ratio of electrons in the external circuit to the number of photons absorbed in the active layer. IQE and QE give insight into both the charge carrier generation and transport processes in a solar cell.

2.3.3 Equivalent Circuit Model

Before we start the discussion of the electrical properties of organic solar cells, it is important to understand the electrical model of a solar cell. In the ideal case, a solar cell can be modeled by a diode parallel with a current source. But in practice, a series and a shunt resistance should be added to the model such that; the shunt resistor R_{sh} is due to recombination of charge carriers near the dissociation site and the series resistor R_s considers mobility of the specific charge carrier in the respective transport medium.(Figure 2.8) In the ideal case, $R_s = 0$ and $R_{sh} = \infty$.

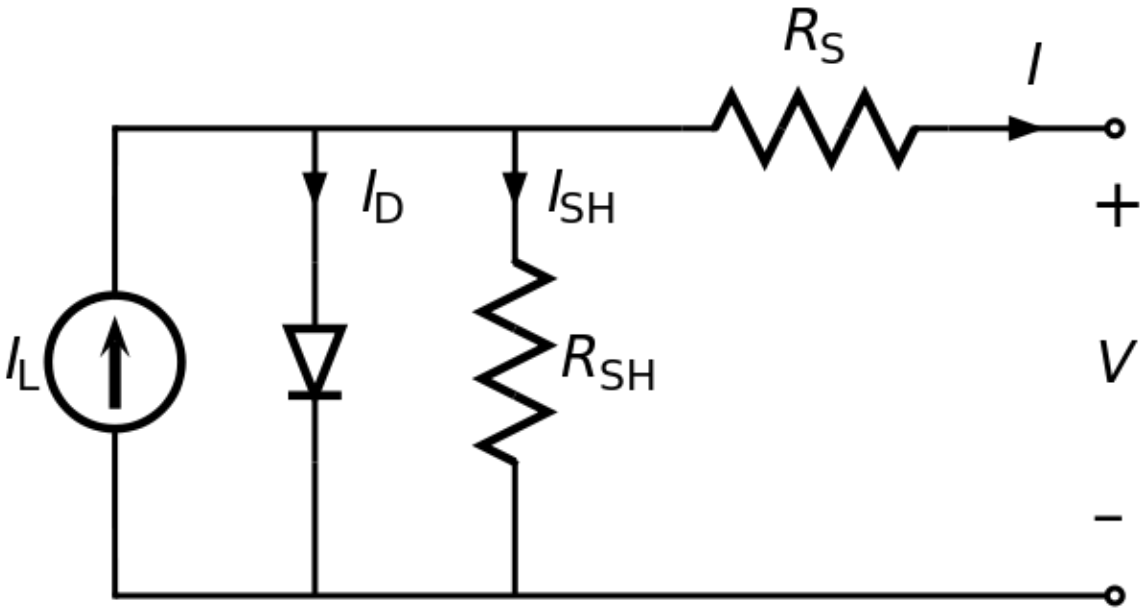

Figure 2-8 Diagram of the equivalent circuit of a solar cell. [41]

The illuminated current density equation is given by,

$$J = J_0 \left[exp \left[\frac{q(V - JAR_S)}{nk_B T} \right] - 1 \right] + \frac{V - JAR_S}{R_{sh}A} - J_{ph} \quad (2.5)$$

where J_0 is the reverse saturation density, q is the elementary charge, A is the active area of the device, n is the ideality factor, k_B is the Boltzmann constant, T is the temperature of the device and V is the externally applied bias voltage [42]. Here, J_{ph} is the photogenerated current density.

2.3.4 I-V curve parameters

The main performance evaluation of a solar cell is described from its power conversion efficiency (PCE). PCE of a solar cell is determined for the current density-voltage characteristics of the cell. The current-voltage characteristics of a solar cell in the dark and under illumination are shown in Figure 2.9.

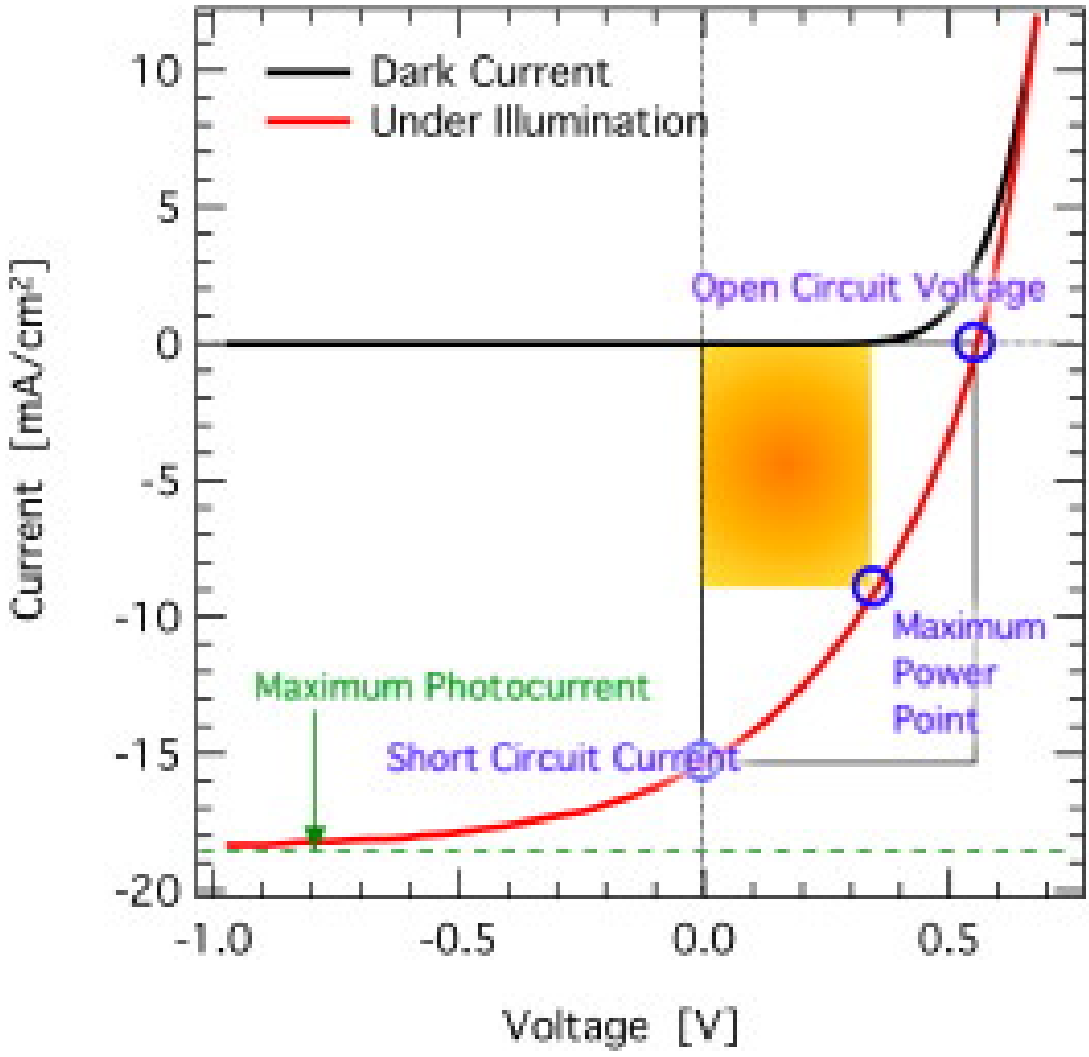

Figure 2-9 Current-voltage (*I-V*) curves of an organic solar cell under dark (black) and illumination (red) [43]

While, the I-V curve shows a diodic behavior in the dark; under illumination, extra charge carriers are generated in the solar cell and the dark IV-curve is shifted in the negative direction. Under illumination, three key figures are determined from the I-V curve; open circuit voltage, short circuit current and maximum power point.

(i) Open circuit voltage (V_{oc});

In organic solar cells, the open circuit voltage is found to be linearly dependent on the HOMO level of the donor and LUMO level of the acceptor [44, 45]. However, this relation is only valid when the electrodes form ohmic contacts with the HOMO of the donor and the LUMO of the acceptor. This relationship can be described by the following equation;

$$V_{oc} = HOMO(D) - LUMO(A) - \frac{kT}{q}\ln[\frac{(1-P)\gamma N_C^2}{PG_M}] \quad (2.6)$$

in which q is the elementary charge, P is the dissociation probability of a bound electron–hole pair into free charge carriers, GM is the generation rate of the bound electron-hole pairs, g is the Langevin recombination constant, N_c is the effective density of states, k is the Boltzmann constant, and T is the temperature [46].

In the solar cell architecture, V_{oc} is dependent on various structural parameters. If the charge carrier loses increases V_{oc} decreases. Moreover, open circuit voltage is dependent on the nanomorphology if the polymers in the active layer. It is also important to have a better match between the metal electrode and the organic semiconductor. This

match is modified by depositing a thin layer of Lithium Floride (LiF) layer between the electrode/polymer interface. This deposition decreases the interfacial effects at the interface.

(ii) Short circuit current (I_{sc});

In the ideal case, photogenerated current of the organic polymer layer in a solar cell can be described by;

$$I_L = ne\mu E \tag{2.7}$$

where *n* is the density of charge carriers, *e* is the elementary charge, μ is the mobility, and *E* is the electric field [47]. When the overall solar cell structure is considered, this current is reduced by several factors. As an outcome, overall short circuit current of a solar cell is described by [48];

$$I_{sc} = I_L - I_{sh} - I_d \tag{2.8}$$

where I_{SH} is the shunt current and I_L is the photogenerated current and I_d is the diode current.

(iii) Fill Factor (FF);

As can be seen in Figure 2.9, maximum power point is the point on the I-V curve under light condition where the solar cell can produce its maximum power. The voltage

and the current at the maximum power point are shown in equation 2.9 as with V_m and I_m , respectively. The ratio of this power power P_{max} to the short circuit current and the open circuit voltage the product is called the fill factor (FF) [34];

$$FF = \frac{V_m I_m}{V_{oc} I_{sc}} \tag{2.9}$$

In the ideal solar device where all the incident power is being converted to the electricity, the fill factor must be unity. However, due to various losses in the device structure this value lies between 0.2 - 0.7.

Fill factor of a solar cell is mainly determined by charge dissociation, the charge carrier transport, and the recombination processes. These processes effect the hole transport capability. When hole and electron transport are unbalanced, a build up space charge region results in the active layer, resulting in low fill factors.

The photovoltaic power conversion efficiency (η) [49] can be calculated with a known incident light power of light as;

$$\eta = \frac{P_{out}}{P_{in}} = \frac{V_{oc} I_{sc}}{P_{in}} FF \tag{2.10}$$

where P_{in} is the incident light power density. This light intensity is standardized at 1000 W/m^2 with a spectral intensity distribution matching that of the sun on the earth's surface at an incident angle of 48.2°, which is called the AM 1.5 spectrum [50].

Chapter 3:

Improve the Hole Collection Efficiency with DNA and Metalized DNA in P3HT-Fullerene Heterojunction Solar Cells

3.1 Introduction

Polymer based solar cell devices have recently drawn tremendous attention for their important advantages over silicon-based solar cells.[35, 51, 52] Bulk heterojunction (BHJ) structure is the state-of-art in the so called 'plastic' solar cells because of their cost effective fabrication procedures, tunable optical properties and promising large area fabrication. The active layer of BHJ is fabricated by cascading solutions of two semiconductors such as conjugated polymers, fullerene derivatives or nanoparticles. Despite of their promising benefits, the efficiencies of BHJ solar cell devices are limited due to several drawbacks: short exciton diffusion lengths of the materials in the active layer [53], short drift length of the charge carriers [54] and non-ordered phase separation [55]. Recently, nanostructures including carbon nanotubes [56], nanorods [57], nanoparticles [58] and nanowires [59] have been utilized to tackle with these issues. Although, the so called hole conducting electrodes increase the charge collection and carrier mobility, their performance is limited due to various factors: What mainly affects their performance are processing bottlenecks for 1D nanostructures and the high recombination rate, especially for nanorods and nanoparticles. In this sense, research using disparate materials can provide promising results, hence an alternative approach is suggested to introduce metallic 1-D nanostructures. These materials can be used as exciton dissociation centers and as ballistic conduction agents with high carrier mobilities. However, the utilization of such nanowires

is scarce because of their limited optical transparency and flexibility. As an alternative, a new nanostructure based on metallized DNA complexes is presented in this paper.

DNA templated nanostructures are optically transparent, flexible and environmentally friendly, and they have similar charge properties as DNA which causes them to act as hole collecting centers. The success on layered assembly of DNA templated Pt nanowires depends on the optimization of their chemical functionalization, individualization and concentration in the organic composite.

In this chapter, a novel method of utilization of DNA and metalized DNA in poly(3-hexylthiophene-2,5-diyl)-[6,6]-phenyl-C61-butyric acid methyl ester (P3HT-PCBM) BHJ solar cells and their optical and electrical characterization is being reported.

3.2 Materials and Methods

BHJ Fabrication: The cell fabrication started with the pre-cleaning of the ITO coated glass substrates from Delta Technologies (15 Ω/sq) by sonication in de-ionized water, acetone, isopropanol alcohol in 10 minutes each and and subsequent rinsing. After this pre-cleaning, 5 min. O_2 plasma treatment is applied to the surfaces to remove the organic particles on the surface. Benefits of this plasma cleaning on the series resistance have been previously shown [60]. After the plasma treatment, a thin layer of PEDOT:PSS (Baytron P) was spin-coated from aqueous solution at 4000 rpm for 40 s, after passing through 0.45 μm syringe filter. The coated substrate was then baked at 150°C for 15 minutes in air. Following this, DNA or Pt-DNA networks were spray-coated onto the substrate using DNA or Pt-DNA solutions where the preparation procedures were

explained in the following paragraph. Then, the samples are dried in argon-filled covered glass petri-dishes. Next, a mixture of 15mg (P3HT) and 15mg (PCBM) blend was dissolved in 1 ml 1,2-dichlorobenzene(ODCB), and stirred for 12 hours at 60°C. This polymer blend was deposited on top of the DNA or Pt-DNA layer at 700 rpm for 50 s via spin-coating by passing through a 0.22 μm filter. High temperature annealing treatment was performed in an argon filled glovebox for 30 min at 120 °C. The samples were then cooled back to room temperature within a 30 minute ramp. In the top contact fabrication, a 1 nm thick LiF (Lithium fluoride) layer and 100 nm thick aluminum (Al) layer were subsequently deposited via vacuum thermal evaporation (Temescal BJD 1800). Using a thin layer of LiF layer between the polymer and the metallic contact layers has an improvement on the overall performance by lowering the work function of the Al electrode and protecting the organic layer from the incoming Al atoms during thermal evaporation [61].

DNA Metallization: The metallization process is started with the preparation of the Pt ion solution by dissolving K_2PtCl_4 (Sigma-Aldrich) and sonicating for several minutes. Then, the solution is kept for aging for 24 hours. After mixing 1mM of the K_2PtCl_4 solution with 5μg/mL λ-DNA solution (Sigma-Aldrich), the reaction mixture is incubated at room temperature for different time periods (5, 12 and 20h) to observe the effect of activation time on the uniformity and size of Pt particles. Afterwards, the reduction process is started by adding 100 μL dimethylaminoborane (DMAB, Sigma-Aldrich) solution to 1 mL of the DNA/Pt solution, followed by heating to 37°C. After 30 minutes, the reduction process is quenched by diluting the solution, followed by sonication for 5 min [62].

IV Measurements: The IV measurements are performed under AM 1.5 G, 1 sun light source (Newport 96000 solar simulator). The J-V characteristics were measured with a probe station and parameter analyzer (Agilent 4155C). EQE measurements which are used to calculate IPCE are performed using a 150W Xenon lamp with 10 band pass filters which are in the range of 350 nm and 800 nm.

C-V Measurements: A DNA layer is formed by spray coating of λ-DNA on a p-Si substrate. Then, both silicon and DNA coated silicon substrates are spin-coated with PMMA (Microchem, 950 A4) for 40 s at 4000 rpm which results a 200 nm layer. After annealing at 70°C for 30 min, Al is evaporated on top as a contact for the device. Measurements are taken using LCR meter at 100KHz. (Agilent 4284A)

Microscopy: AFM characterization is done by Veeco Multimode V. Samples were coated with Au/Pd composite and Scanning Electron Microscope (SEM) images were obtained at 5 kV(Leo 1550 FE SEM).

3.3 Results and Discussion

As shown in Figure 3-1 (a), three different devices are fabricated. In device 1 (control), ethylene-dioxy-thiophene:polystyrene sulfonate (PEDOT:PSS) and P3HT:PCBM thin films are spray-coated on top of ITO coated glasses. Fabrication of device 2 (DNA) and 3 (Pt-DNA) included the coating of DNA and DNA templated Pt nanowire layers respectively on top of the PEDOT:PSS layer to provide a similar effect that was observed with the incorporation of single walled carbon nanotubes [63, 64]. The energy-level diagram in Figure 3-1 (b) indicates the highest occupied molecular orbital

(HOMO) energies and the lowest unoccupied molecular orbital (LUMO) energies of the individual materials including the DNA [32] and Pt [65] work functions. Here, since Cyclic Voltammetry (CV) is used to calculate the exact work function of the Pt-DNA complexes, a reliable information cannot be extracted. However, due to the increase in the performance of the devices, it is assumed that the work function lies in be between the DNA and the Pt work functions[66]. How these materials contribute to the hole collection by performing a graded layer passage can also be realized from this diagram.

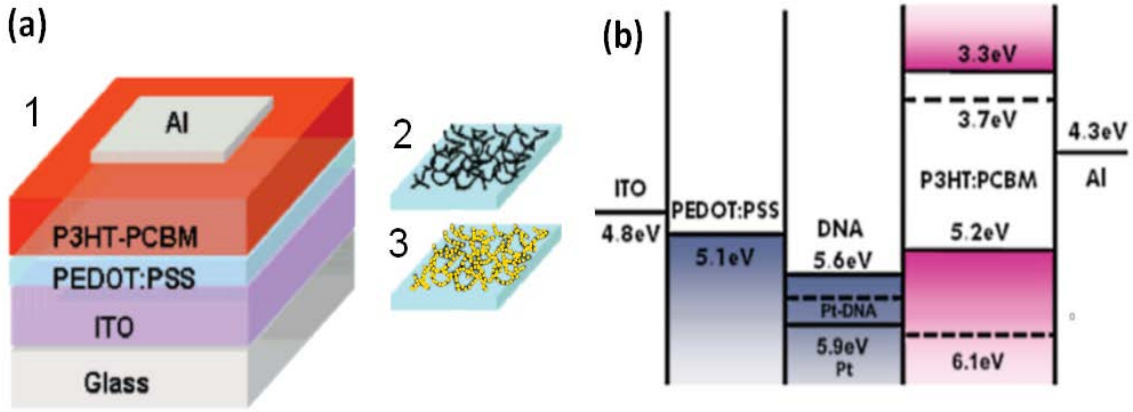

Figure 3-1 (a) Schematic of device showing when DNA (device 2) and DNA-Pt (device 3) incorporated (Adapted from [67]), (b) Energy band diagram of the SC device including the DNA and the Pt-DNA layers (Adapted from [35])

Figure 3-2 (a) shows the absorbance of the defined devices. Based on prior research, DNA has poor absorption in the visible region[68]. So, the addition of a DNA layer to the control device results in only a slight increase in the visible region of the absorption spectra. In the case of metalized DNA, the binding of Pt complexes to the bases of the DNA strands [69] suppresses the absorption of the DNA. As a result, the increase in the absorption spectra for the device becomes less, and becomes similar to the absorption spectra of the

control device. Unlike the effect in the absorption spectra, DNA improves the quantum efficiency between 450nm and 600nm as shown in Figure 3-2 (b). However, when Pt complexes are attached to the DNA sequences, the IPCE of the control device in the visible region is significantly improved, which is based on introducing a material with a lower resistance in the device structure instead of bare DNA.

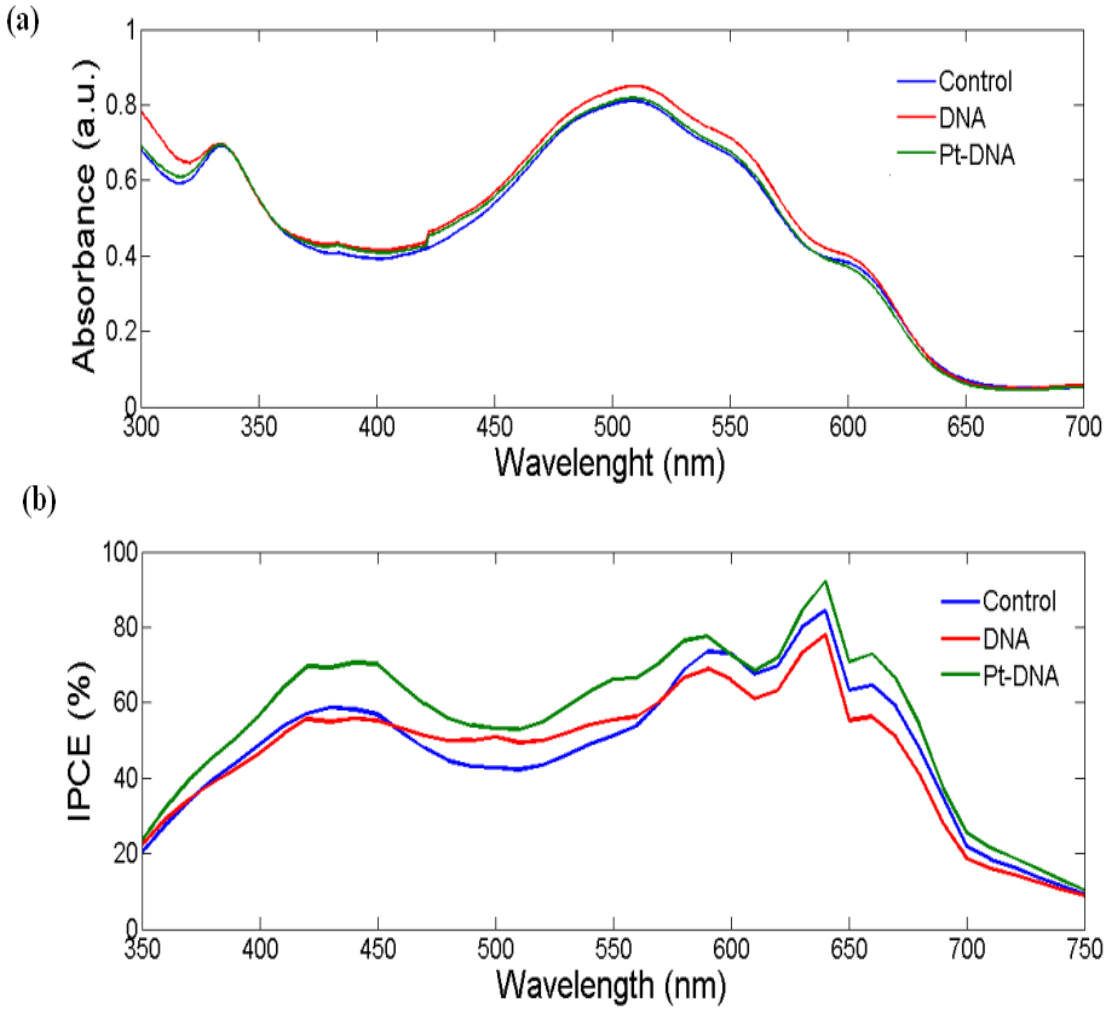

Figure 3-2 (a) Absorbance spectrum of the Control, DNA and Pt-DNA devices. (b) IPCE spectra of the Control, DNA and Pt-DNA devices

The results of the I-V measurements are given in Figure 3-3. Table 1 provides a summary of the short circuit current, the open circuit voltage (both determined from Figure 3-3), fill factor (FF) and the power conversion efficiency (η), which are calculated [49] under AM 1.5 G, 1 sun illumination. According to these results, a %16 increase is observed in the PCE of the control device when DNA fragments are incorporated on the PEDOT-PSS layer. Furthermore, when the DNA templated Pt nanowires are placed on the PEDOT:PSS layer, a %30 increase in the PCE is observed. Although these efficiency values were affected from air contamination during the fabrication and characterization processes, these observed increases on the overall efficiencies are significant. In addition to improvement in the efficiencies, further improvements in the I_{sc} values are also noticed. The improvement in the I_{sc} values can be explained by the enhancement of hole transport [70] provided by the DNA network. Although this network maximizes the surface area for charge collection, the V_{oc} value is not affected from this increase. This is because the V_{oc} value is found to be linearly dependent on the HOMO level of the donor and the LUMO level of the acceptor. Also, there is a further increase in the I_{sc} in device 3 as compared to device 2. This increase can be explained by the incorporation of metalized DNA, since the active layer resistance decreases where the Pt-DNA network performs a better hole collection process than the bare DNA network.

Table 3-1 Effects of DNA and metalized DNA over the electrical characteristics of the organic solar cell devices when used as an hole collecting materials

Device	V_{oc} (V)	J_{sc} (mA/cm^2)	FF	η (%)	R_{series}(Ωcm^2)
Control	0.6	8.5	37.7	1.92	5.1
With DNA	0.6	11.22	33.1	2.23	2.5
With Pt-DNA	0.58	12.3	33.5	2.51	2.3

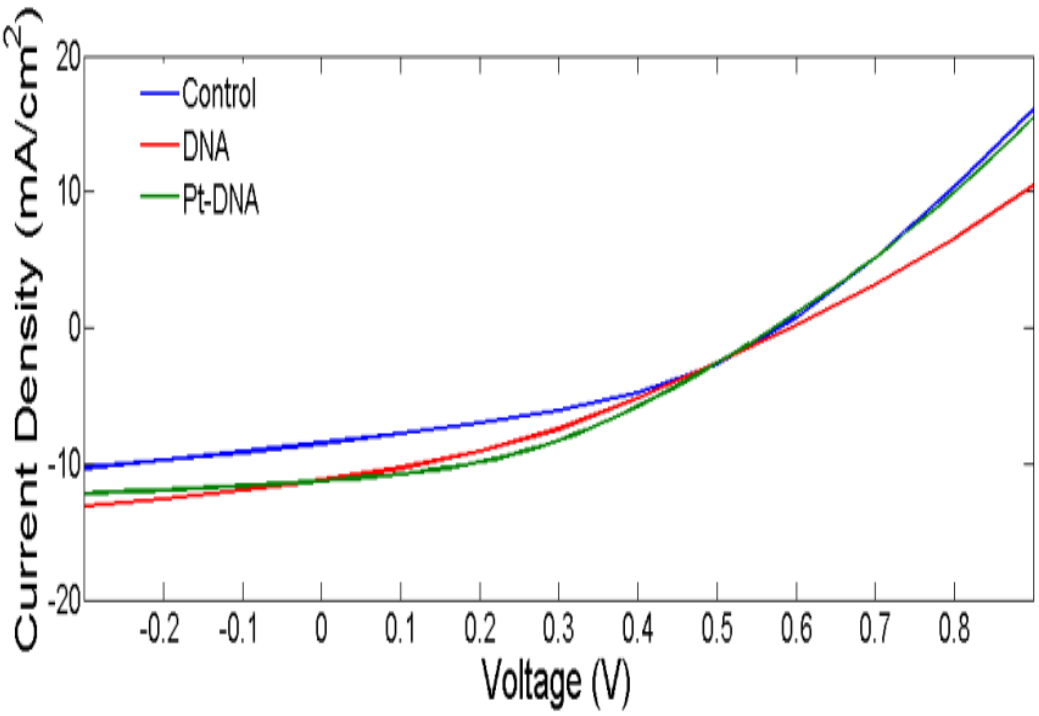

Figure 3-3 Current Density-Voltage characteristics of the Control, DNA and Pt-DNA solar cell devices under AM 1.5 G 1 Sun illumination

The effects of incorporating 1D nanostructures on the device performance can also be explained by introducing a small signal model for the devices [71]. Here, series resistance (R_S) measurements are taken based on equation 3-1 [72]. In this equation, $V_{\max P}$ is the voltage at the maximum power point in Figure 2.9, $I_{\max P}$ is the corresponding current at the maximum power point, I_L is the light-generated current, K_B is the Boltzmann constant, T is the temperature of the device and A is the diode factor. According to the results in Table 1, the improvements are also reflected in the R_S values of the devices, where devices 2 and 3 show R_S values of 2.5 and 2.3 Ωcm^2, respectively, which are lower than that of the control device (Device 1, 5.1 Ωcm^2). The increase in the I_{sc} values is mainly affected by this decrease in the R_S values.

$$R_S = \frac{V_{\max P}}{I_{\max P}} - \frac{AK_BT}{q\left(I_L - I_{\max P}\right)} \tag{3.1}$$

Table 3-1 indicates that the introduction of metalized DNA led to further improvements on the performance of the device over the introduction of DNA. Fabrication of metalized DNA complexes is based on heterogeneous nucleation of metal nanoparticles on the DNA strand. During fabrication, Lambda phage DNA (λ-DNA) is chosen as the template because it introduces a highly negatively charged layer. Potassium tetrachloroplatinate(II) (K_2PtCl_4) salt is used as the source of Pt(II) complexes to form the initial phase nanoparticle nucleation. Previous studies showed that it is essential to start the metallization process with the activation of the DNA bases followed by the reduction of

the Pt(II) complexes [73]. In the activation step, the complex Pt ions bind to the DNA bases with covalent bonds [69] and serve as nucleation sites for the subsequent cluster growth. Then, the Pt clusters are reduced to the metallic nanoparticles in the reduction step.

During the metallization procedure, assembling of Pt nanoparticles along the DNA template is controlled by several parameters. For this application, we believe that it is required to synthesize cluster chains where the DNA strand is fully covered with metallic nanoparticles. In this way, the ballistic effect on the charge carrier collection of DNA can be increased and the resistive behaviour of the DNA layer in the device can be decreased. An important parameter in the construction of the uniform Pt nanostructures is the duration of the binding process [74]. To achieve this, we investigated the effect of activation time over the cluster formation. The effect of the reduction time on the metallization process is shown via the AFM images in Figure 3-4. Three different samples are considered for three different activation times; 5, 12 and 20 hours, respectively. From the height images shown in Figure 3-4 (a)-(c), we observe that the longer the activation time is, than the better is the metallization process. In Figure 3-4 (a), with the starting of the nucleation process on the DNA strand, agglomeration of Pt clusters forms island shaped nanoparticles on the surface. These large structures are formed with the coherence of highly concentrated Pt ions via drying of the sample meniscus. As the activation time increases, more Pt ions are absorbed along the DNA strands [75]. After 12 hours of activation, the ions form small island shaped clusters on the λ-DNA backbone (Figure 3-4 (b)). The clusters coalesce into a continuous metallic nanowire after 20 hours of treatment (Figure 3-4 (c)). AFM images indicate that

the average diameter of the templated nanowires is 20nm (Figure 3-4 (d)) and the average height of the nanowires is approximately 2nm (Figure 3-4 (d) inset).

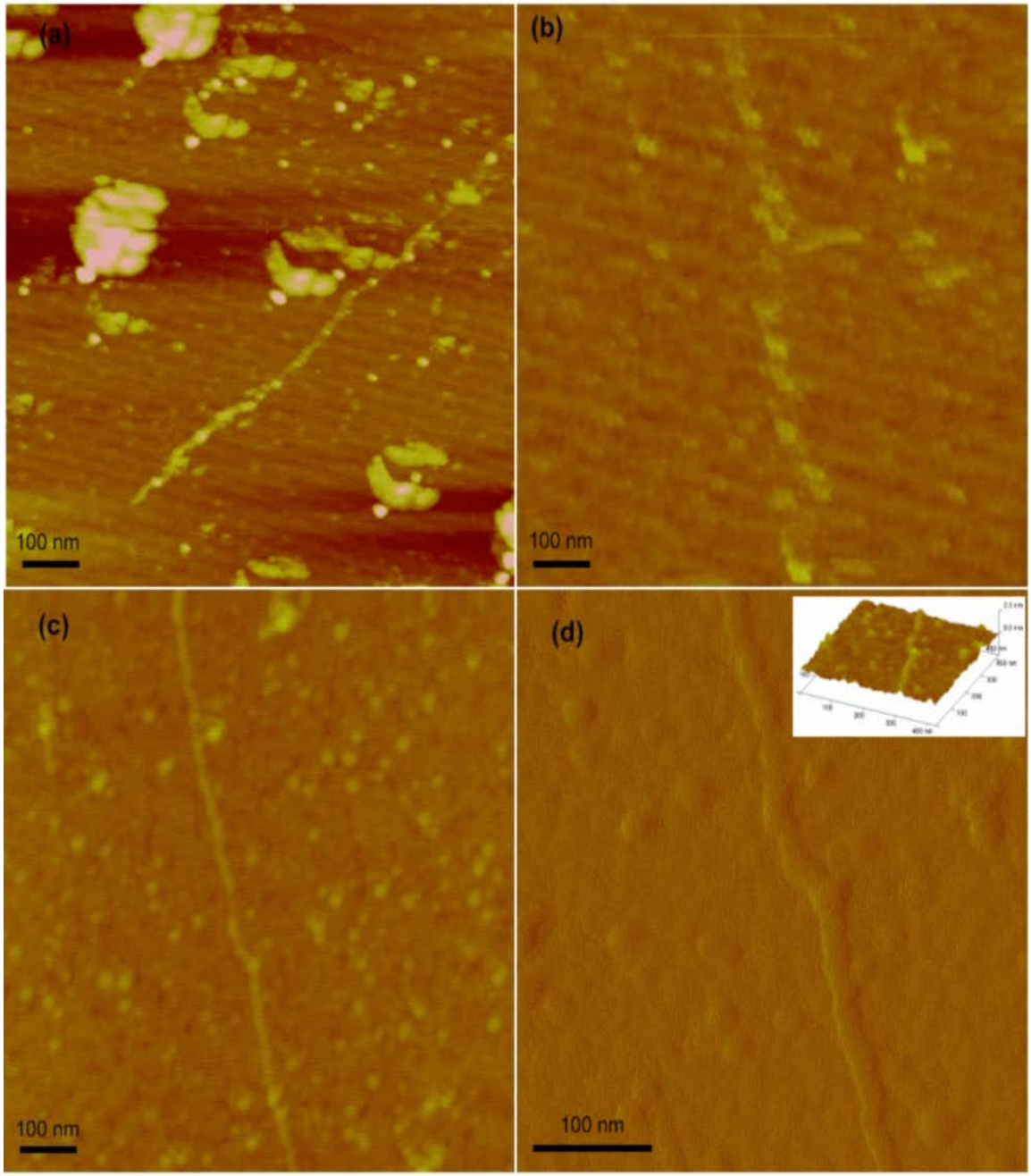

Figure 3-4 AFM images of Pt-DNA strands fabricated at 37°C in a mixture of 1mL Pt/DNA solution and 100µL DMAB for different activation times; (a)5h, (b)12h, (c)20h. A detailed AFM top-down image (d) and height image (d inset) for 20h activation time. [67]

As shown in the SEM images in Figure 3-5, diluted λ-DNA solution was drop casted on the glass cover to form the alignment of DNA molecules [76]. During room temperature evaporation of this droplet, receding water meniscus remains stretched individual DNA molecules on the surface [77, 78]. Since the glass substrate is not conductive, charging effects are minimized by puttering the sample with a composite Au/Pd target for 8 sec.

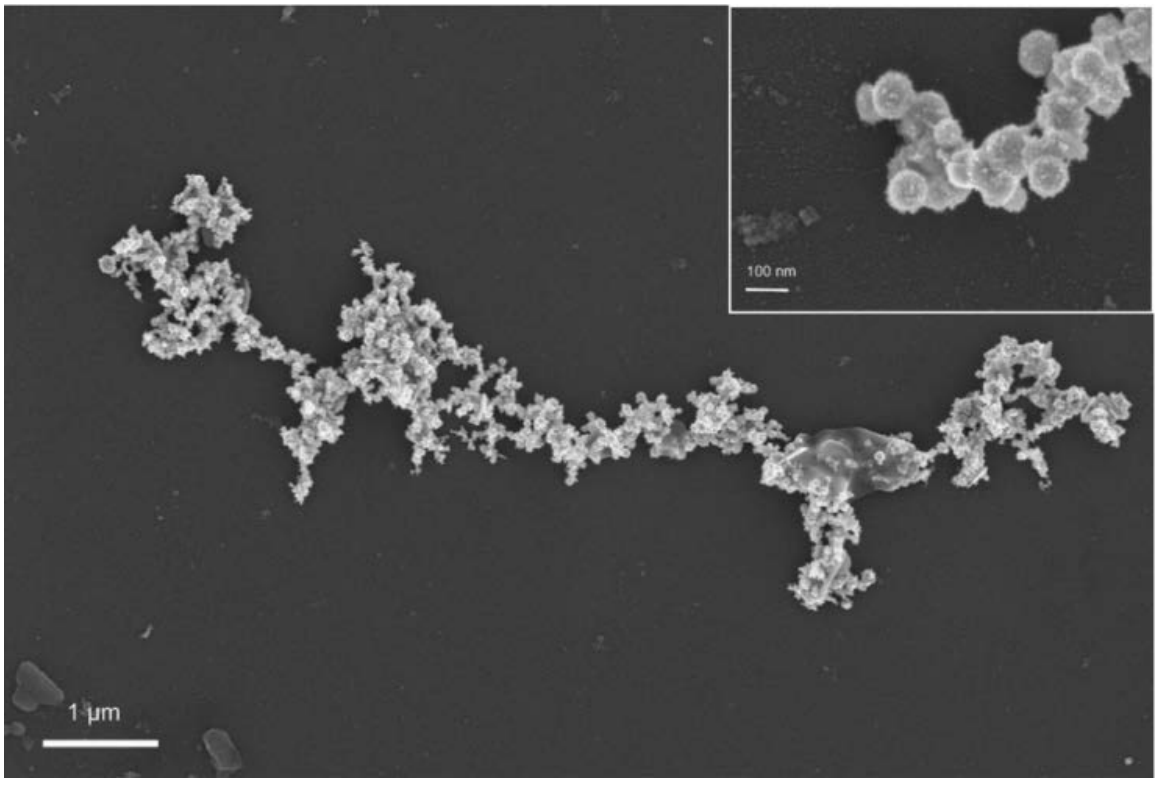

Figure 3-5 Top-Down SEM image of Pt-DNA strand on glass substrate. The substrate is sputtered with composite Au/Pd target to get a detailed SEM images as shown in the inset. [67]

For a better understanding of the efficacy of DNA fragments as hole conducting electrodes, approximate charge density for the DNA is measured. For this measurement,

the fixed oxide charge on a Metal-Oxide-Silicon (MOS) capacitor model is used. Based to this approach, there exists a fixed charge at the oxide-semiconductor interface where the charged DNA layer provides a shift in the flat band voltage by an amount which equals to the charge divided by the oxide capacitance [79]. In our MOS capacitor devices, polymethylmethacrylate (PMMA) is used as the insulating layer and for the sake of simplicity in these measurements, the layer structure of the devices are chosen as p-Si/λ-DNA/PMMA/Al and p-Si/DNA/PMMA/Al [80].

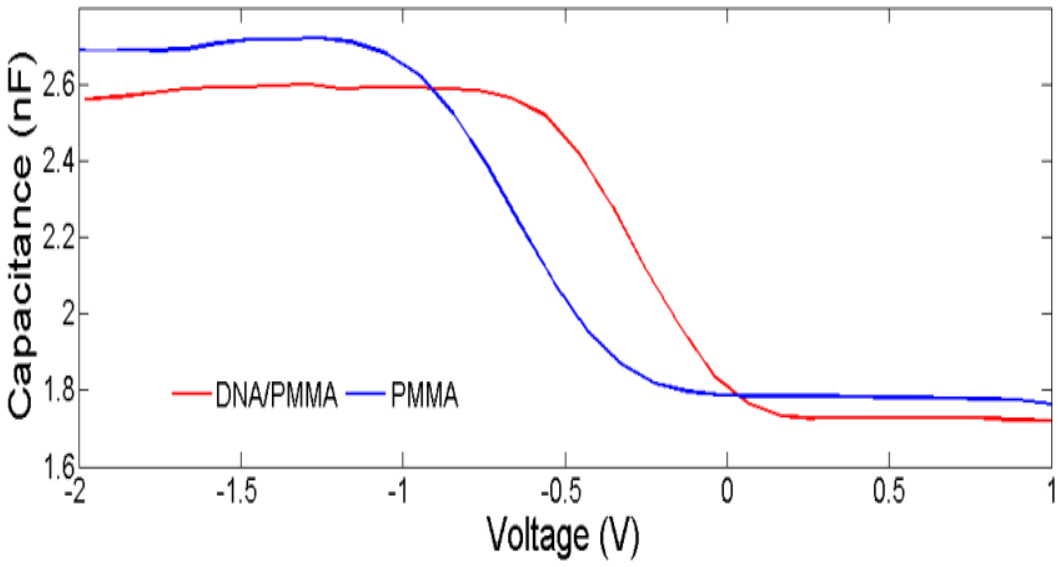

Figure 3-6 Capacitance–voltage (C–V) characteristics of the p-Si/λ-DNA/PMMA/Al and p-Si/PMMA/Al structures at 100 KHz (Area=16mm2).

In these devices, the value of the oxide capacitance can be calculated as 14 nF/cm^2 where the PMMA layer thickness is 200 nm and the dielectric constant is ε=3.2 ε_0.[80] So, the theoretical capacitance value for our device, which has an area of 16 mm^2, can be found as 2.25 nF. According to the measurements summarized in Figure 3-6, total capacitance of

the devices is found as 2.6 nF. Based on the measurements in Figure 3-6, the addition of a λ-DNA layer causes a 0.3V positive voltage shift to the flat band voltage of the p-Si/DNA/PMMA/Al device. So, the charge density of the λ-DNA layer is calculated to be Q=-4.875 nC/cm^2. This result indicates that the spray coated λ-DNA layer introduces a negative charge between the layers which is significant enough to increase the hole collection efficiency in our BHJ device [81].

3.4 Conclusions

We presented a novel approach to incorporate DNA and Pt-DNA networks on the cathode side of the active layer of P3HT/PCBM BHJ PV devices. By coating a layer of DNA and Pt-DNA on the PEDOT:PSS layer, the power conversion efficiency is improved by %16 and %30, respectively. The negative charge of the DNA fragments increases hole collection which in turn increases the short circuit current. The presence of negative charge is confirmed with C-V measurements. These results depict that DNA and DNA template nanostructures can be used in the organic solar cells to improve the device performance. However, further studies on the metallization and layer formation of the DNA are required to increase this performance.

Chapter 4:

Graphene in Organic Solar Cells

4.1 Introduction

The dramatic advances in the last few decades bring many problems with it. In this time, carbon based electronics is introduces as an alternative solution to these problems. The research in carbon based electronics started with three dimension allotropes (diamond, graphite) of carbon. Recently discovered one dimension (nanotubes) and zero dimension (fullerenes) allotropes of carbon increased the interest in carbon electronics. But, as being the most theoretically studied carbon allotropes for many years, graphene was recently able to fabricate.

After various attempts, in the last 50 years, researchers were able to fabricate small size graphene flakes in the beginning of 2000s. After this successful attempt, graphene has become a very hot research topic because of its unique electrical, mechanical and optical properties.

In this chapter, one of these researches based on using graphene as a transparent electrode is discussed. The chapter starts with defining the unique electro-mechanical properties of graphene and follows with the recent fabrication and characterization methods. Later on, the research on the surface functionalization and characterization over

the big graphene flakes are discussed. The results of this project are shown as the evidence of the possible replacement of the up-to-date transparent electrodes with graphene.

4.2 Properties of Graphene

Theoretically, graphene is the most interested and studied carbon allotrope because of its unique material properties. The lattice structure of graphene consists of two interpenetrating triangular sublattices where the carbon atoms of one sublattice are placed in the center of the after sub-lattice. (Figure 4-1) The distance of the carbon atoms in the lattice is 1.42 A.

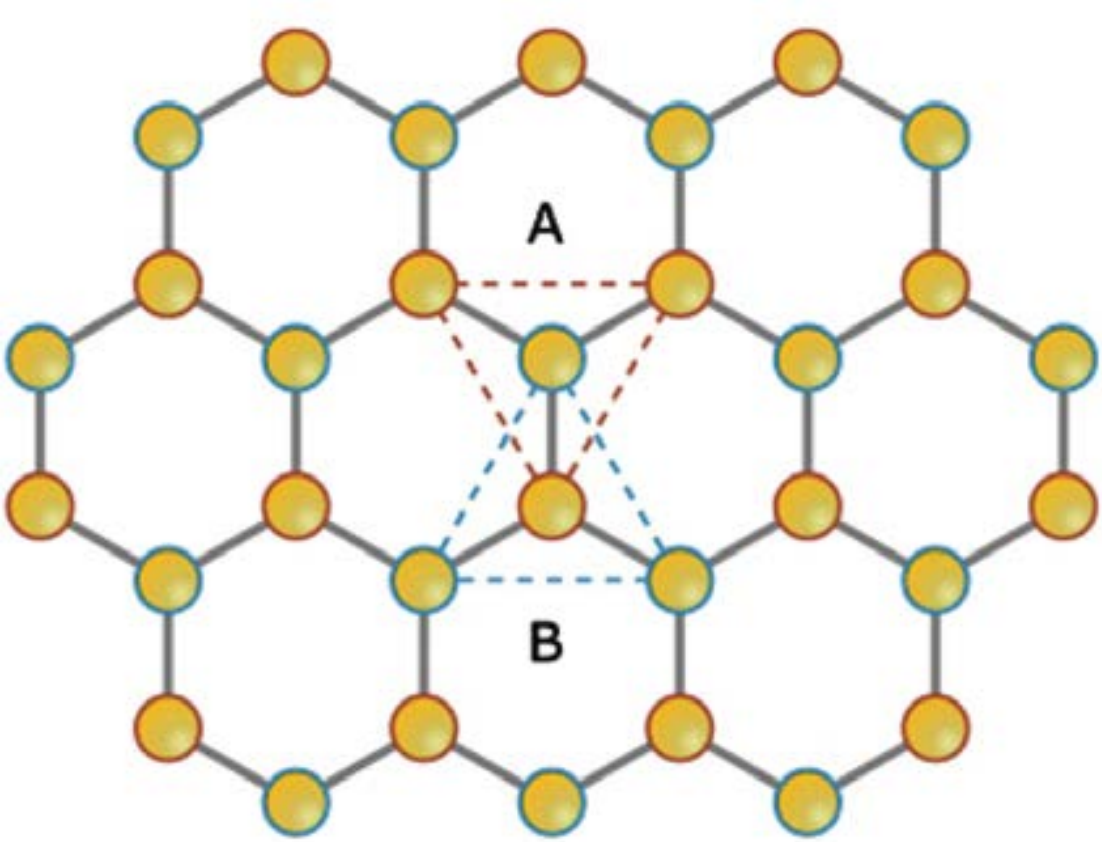

Figure 4-1 Graphene lattice consists of two interpenetrating triangular sublattices, each with different colors [82]

Each atom has one s orbital and three p orbitals; px, py & pz. The s and the planar px and py orbitals hybridize to form a strong covalent sp2 bands. The remaining pz orbital hybridizes with its neighboring carbons to form the π (conduction) and π^* (valence) bands. The electrons on these bands form extremely weak out-of-plane interactions. As a result, electrical and thermal conductivities in the out-of-plane direction are around 10^3 times lower than the in-plane analogues.

4.2.1 Electrical Properties

The electronic structure of graphene can be explained with the nearest neighbor, tight-binding approximation. According to this approximation, electron energy is linearly dependent on the wave vector at the edges of the Brillouin zone. This results the electron to behave with the hopping process.

This band structure property resembles the dirac-like spectrum of the massless fermions. So, similar to the fermions, electrons more with quantum-mechanical hopping process between the sub lattices. As a result; the speed of electrons in graphene is linearly dependent with the speed of light.

Experimental results are also corresponding with the theoretical approximation of the hole and electron mobilities. For the microcleaved deposited graphene, electron mobility exceeds 25000 cm^2/V at room temperature [83, 84]. Experiments also show that the dominant scattering mechanism in graphene is the defects [83, 85]. These defects used

by the graphene itself and the interaction between the graphene and the substrate, are tried to reduce by annealing and suspending the graphene devices, which shows the mobility can exceed 200000 cm^2/V [86-88].

Moreover to the high mobility, linear dispersion curve near the Dirac point leads the Fermi level to be easily set by adjusting the doping level [83, 84, 89-91]. This property with the possibility to open a band gap within the bands allows the graphene FET device fabrication [92].

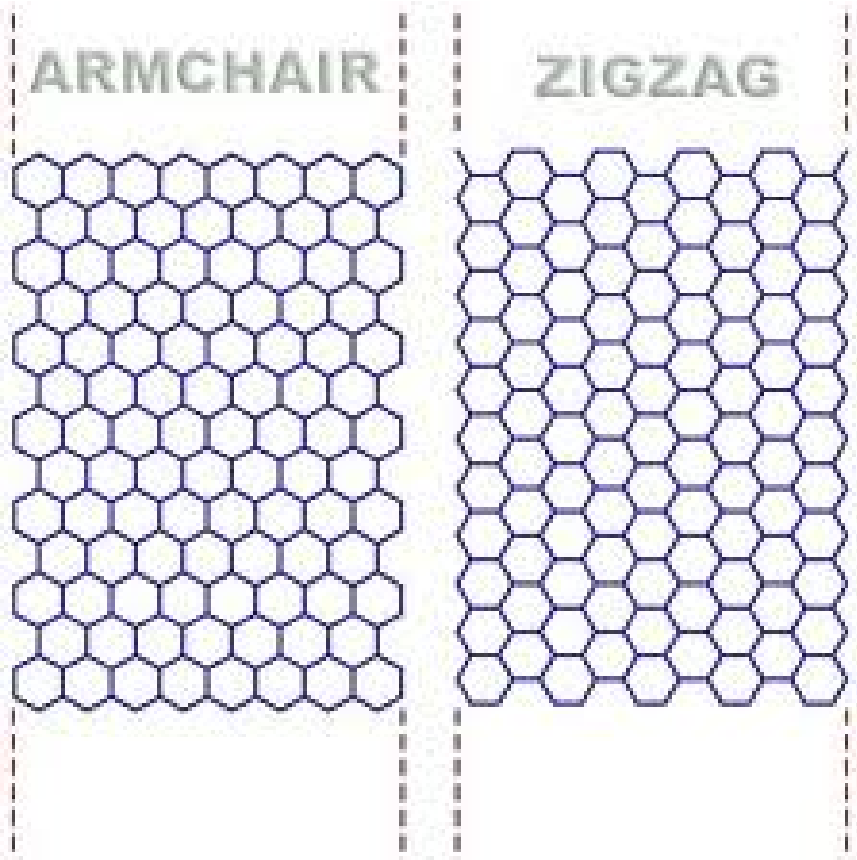

Figure 4-2 Graphene nano ribbons metallic and semiconducting behavior based on its edge morphology [93]

Graphene FET devices are first proposed with the ribbon shaped graphene devices. In these devices graphene was laterally confined in two degrees and graphene nano ribbons (GNRs) metallic and semiconducting behavior based on its edge morphology [94, 95]. Calculations based on tight binding predict that zigzag GNRs are always metallic while armchairs can be either metallic or semiconducting, depending on their width. (Figure 4-2)

In addition to these unique properties, availability of the large graphene growth leads as a candidate for the transparent electrode applications. Several attempts show that large area graphene can be fabricated with the reduced sheet resistance and high transparency [96, 97].

4.2.3 Mechanical properties

Similar to the other carbon allotropes, graphene has unique properties in terms of mechanical robustness, Young's modulus or be it hardness. Stiffness of the graphene sheet is found of the order of 300-400 N/m by using AFM nano indentation [98]. Some studies show that breaking strength of ca. 42N/m represents the intrinsic strength of a defect-free sheet. Having such a high tension in a single sheet makes graphene a strong material for various NEMS applications such as resonators or pressure sensors. One of the recent studies shows that suspended graphene provides membrane for gas sensing applications [99].

4.2.3 Optical Properties

As a single layer, graphene is a highly transparent material. It has been shown that sub-2nm thick suspended graphene films yield >95% transparency [96, 97, 100]. Also, large area CVD growth graphene sheets have >80% transparency [101] for single layer and remains about 80% for 5 layer sheets [102, 103]. (Figure 4-3) The results show that transparency of the graphene films linearly decreases with the number of layers in a visible range. The results also show that on a few layer range, introducing another layer decreases the transmittance by around 2%. This constant in this linear behavior of the transparency can be explained with the coupling between light and relativistic electrons [104].

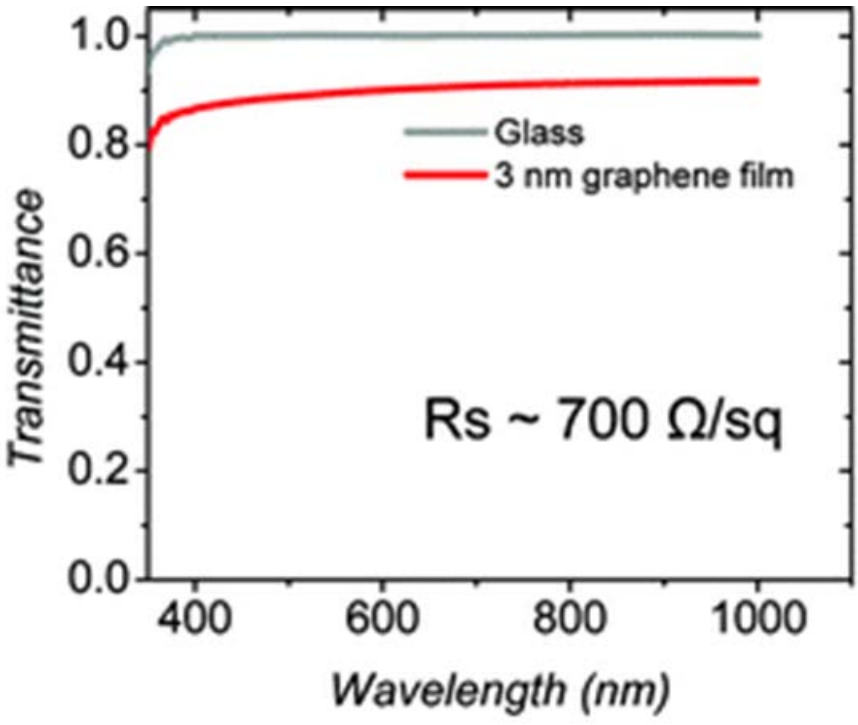

Figure 4-3 Optical transmittance of a graphene film with 3 nm average thickness on glass.[105]

4.3 Fabrication Methods

Although theoretically studied in detail, utilizing fewer layers of graphene was not possible until recently. First researchers came up with couple of different approaches to form few layers of graphene. In 1999, Ruoff's group came up with an approach to use AFM tip to manipulate small pillars into highly oriented pyrolytic graphene by plasma etching. With this approach, they were able to form around 600 layers of graphene [106]. Later on, Kim's group improved the method to form ~30 layers [107].

4.3.1 Mechanical Exfoliation

Although these approaches were able to form multilayer graphene samples, the most remarkable approach developed by Novaselov and Geim's group in 2004 [108]. In this most basic form, the so called mechanical exfoliation method consists in using common cellophane tape to repeat the peeling process multiple times to remove layers from graphite flake.

During this peeling process, van der Waals attraction between the graphene and the substrate can delaminate a single layer when the tape is lifted. Although the success rate of forming a single layer is depend on the experience, it is possible to form single flakes of 100 μm^2 in size.

The Manchester group also shows that using a SiO_2 (with a specific thickness of 300mm) on Si helps to enhance the visualization of graphene flakes on the substrate [109].(Figure 4-4)

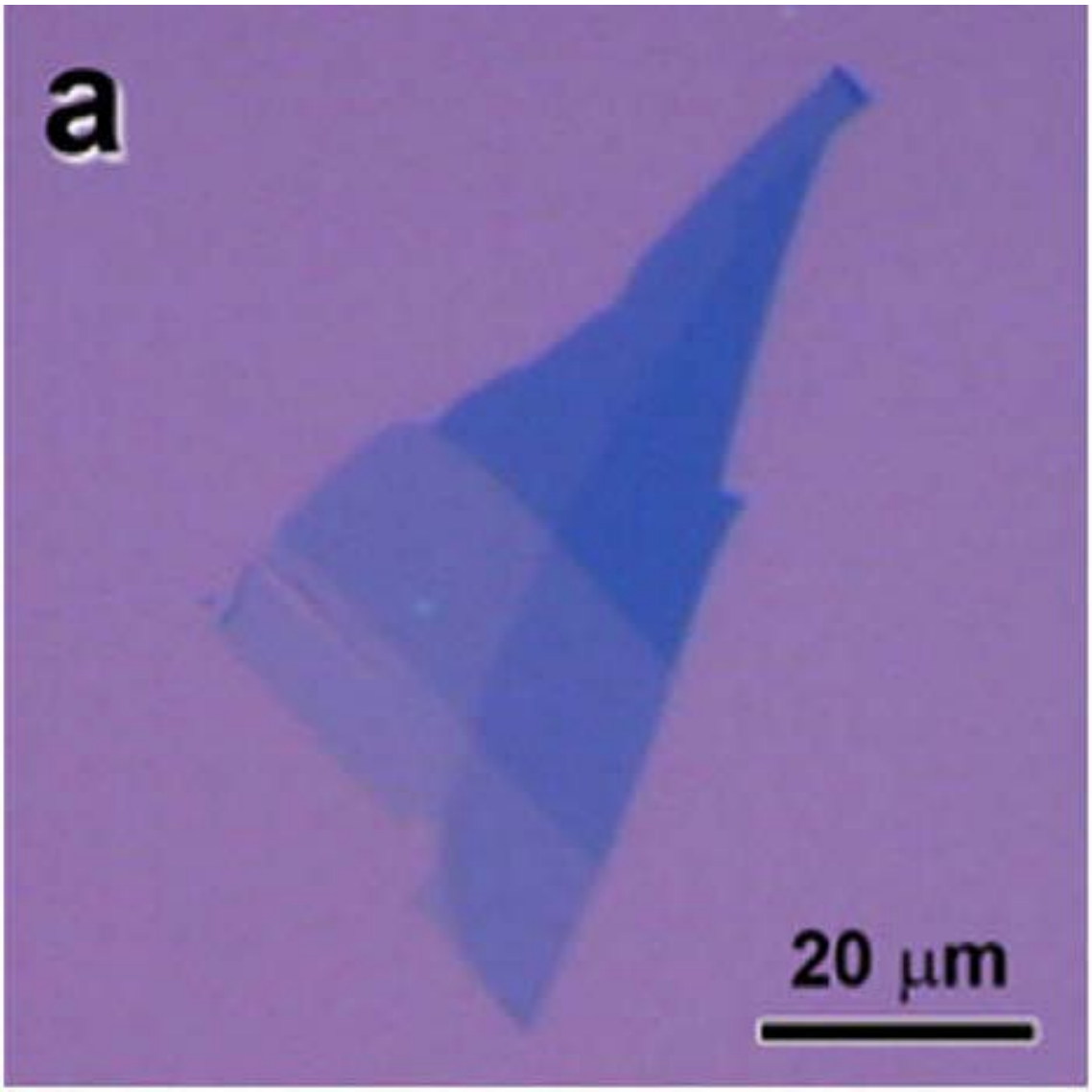

Figure 4-4 Optical microscopy image of micromechanically exfoliated graphene [82]

Although this method made a great impact on the experimental graphene research, having a low throughput and scalability problems led the researches to find alternative routes.

4.3.2 Chemically derived Graphene from Graphite Oxide

The graphene synthesis research is based on three important factors to be used in real world devices. First of all, the process must produce high quality graphene samples. Second, the method must provide fine control over the crystalline thickness. And finally, the outcome must be compatible with the state of the art fabrication processing.

Keeping these factors in mind, Ruoff's group was able to demonstrate a solution-based graphene fabrication method in 2006 [110-113]. The method is based on a chemical exfoliation process of graphite oxide and removing the oxygen groups by chemical treatment.

In detail, the process starts with weakening the van der Waals bonds between the layers. This is done by oxidation of the graphite producing less aromatic carbon groups. After that, oxygen groups are removed either chemically by using hydrazine hydrite [111] or thermally by rapid annealing to 1050°C [114-116].

In spite of the promising progress of chemical exfoliation, the efficiency of graphene is still a problem that must be solved. Until now, the chemical derived methods were able to form resulting materials which contain both graphine and number of layers and layer size. Also, it is not possible to address the graphene to the desired positions because it is a solution-based process.

4.3.3 Substrate based graphene growth

Addressing the problems of the previous two methods, researchers came up with two different approaches which are based on growing graphene directly on solid substrates. One of approaches uses thermal decomposition of carbides. De Heer group show that high temperature reduction of silicon carbide results graphene layer [117-119]. They showed that desorbing silicon carbide in ultrahigh vacuum and around 100°C leaves small graphene islands behind. (Figure 4-5)

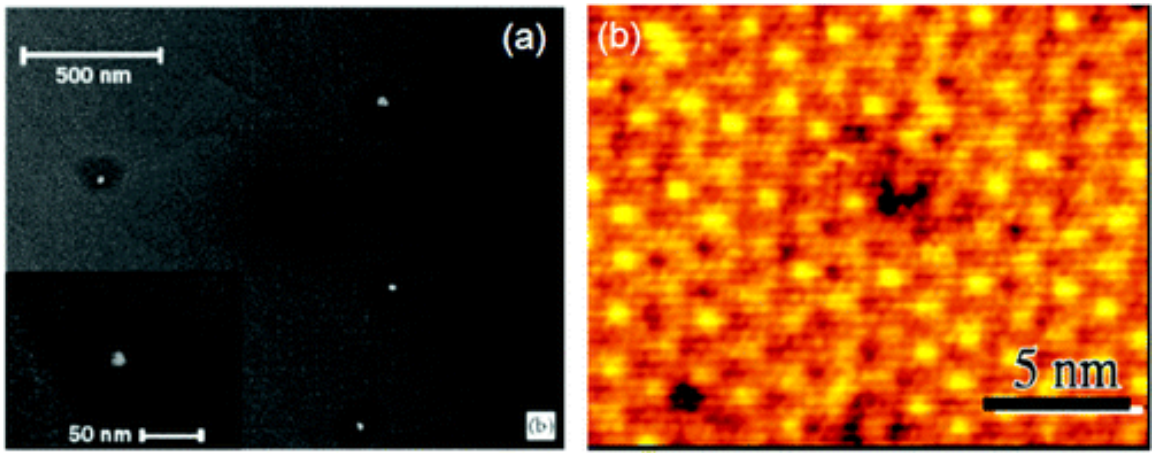

Figure 4-5 Silicon carbide is reduced to graphene as silicon sublimes at high temperature. (a) SEM image shows small hexagonal crystallites. (b) STM image shows long-range order and a low density of defects. [120]

Further research results show that it is possible to grow wafer-scale montage graphene by a higher annealing temperature [121, 122]. These promising results increased the attention on this method in the last years.

The other substrate-based growth method is Ultra High Vacuum (UHV) chemical vapor deposition (CVD) on single crystal transition metals [123]. This process is pioneered by groups from Korea and MIT. The method relies on the carbon saturation on the metal catalyze surface at high temperatures. Hydrocarbon gases, such as, methane or ethylene can be used as the source gas. Another important parameter is the type of the substrate material. In literature, CVD growth process is studied on various single crystalline metals such as Ir [124, 125], Co [126], Ru [127, 128], Ni [129-131], Pt [132] and Cu [133, 134]. Among these materials Ni and Cu gave very promising results especially in the field of large are graphene growth.

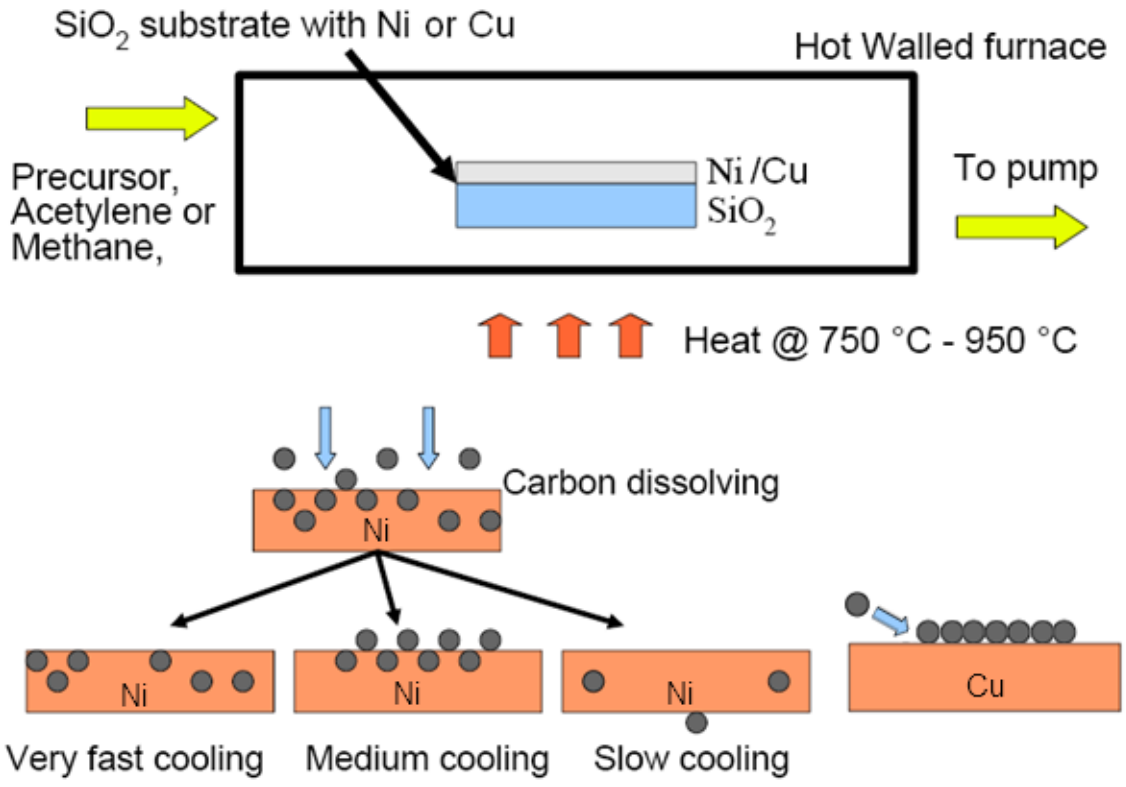

Figure 4-6 Schematic of CVD growth graphene mechanisms on Ni and Cu substrates [135]

When the growth process is studied in detail for Ni and Cu substrates, graphene formation is different for two metals. (Figure 4-6) For Ni substrate, graphene is grown due to C segregation or precipitation process. The most important parameter in the process is the cooling rate.

Although it is possible to grow single layer of graphene with Ni substrate, lack of control over the growth parameters limits its efficiency and uniformity. This problem is overcome by changing the substrate to Cu. Graphene films grow on Cu substrate by a surface adsorption process. This process automatically yields one layer graphene. Also large area few layer graphene can be grown layer by layer with Cu substrate.

4.4 Characterization Methods

Fast and accurate characterization of graphene is as important as the fabrication of it. For an efficient characterization, various techniques are proposed in the literature, such as; optical microscopy, AFM TEM and Raman scattering.

Optical microscopy is based on maximizing the optical contrast between the substrate and the monolayer of the carbon atoms. In the literature, the appropriate substrate is found as oxide coated silicon wafers where the thickness of the SiO_2 layer is found as 300 nm [108]. By adjusting the thickness such that, the reflected light intensity is maximized at about 550nm which gives a distinct contrast difference especially in the green channel display.

One of the first techniques for the characterization is AFM. Although it is difficult to be used for the identification, it gives a better understanding for the topological quality of the samples [136]. Different parameters are important for the AFM technique such as, SiO_2 substrate roughness, AFM tip quality, ambient noise and ambient humidity. Being too slow and limited in the scan size are the main disadvantages of this technique.

Another characterization tool is the TEM [137, 138]. Although it has the best resolution and gives the most accurate information about the graphene lattice and the quality, difficult and long sample preparation procedure limits its convenience.

The most efficient technique is using Raman scattering [139, 140]. The technique provides insight information on the electron-phonon interactions. It has been extensively used for the carbon materials for the last 20 years [141].

By changing the wavelength of the incident phonons, scattered phonons are collected. The intensity of the scatted phonons changes by the change of the frequency of the incident phonons. This intensity vs frequency graph is unique for all materials and gives an insight information about the material. For graphene, the appropriate wavelength range is from 800 to 2000 cm^{-1} and in this range Raman scattering of the graphene has two unique peaks [140]. (Figure 4-7)

The G peak, around 1500 cm^{-1}, corresponds to the E_{2g} phonon at the center of the Brillouin zone. Moreover, the defects or the smoothness of the graphene substrate can be determined by the D peak. The D peak, around 1350 cm^{-1}, is due to the out-of-plane breathing mode of the sp^2 atoms and is active in the presence of defects.

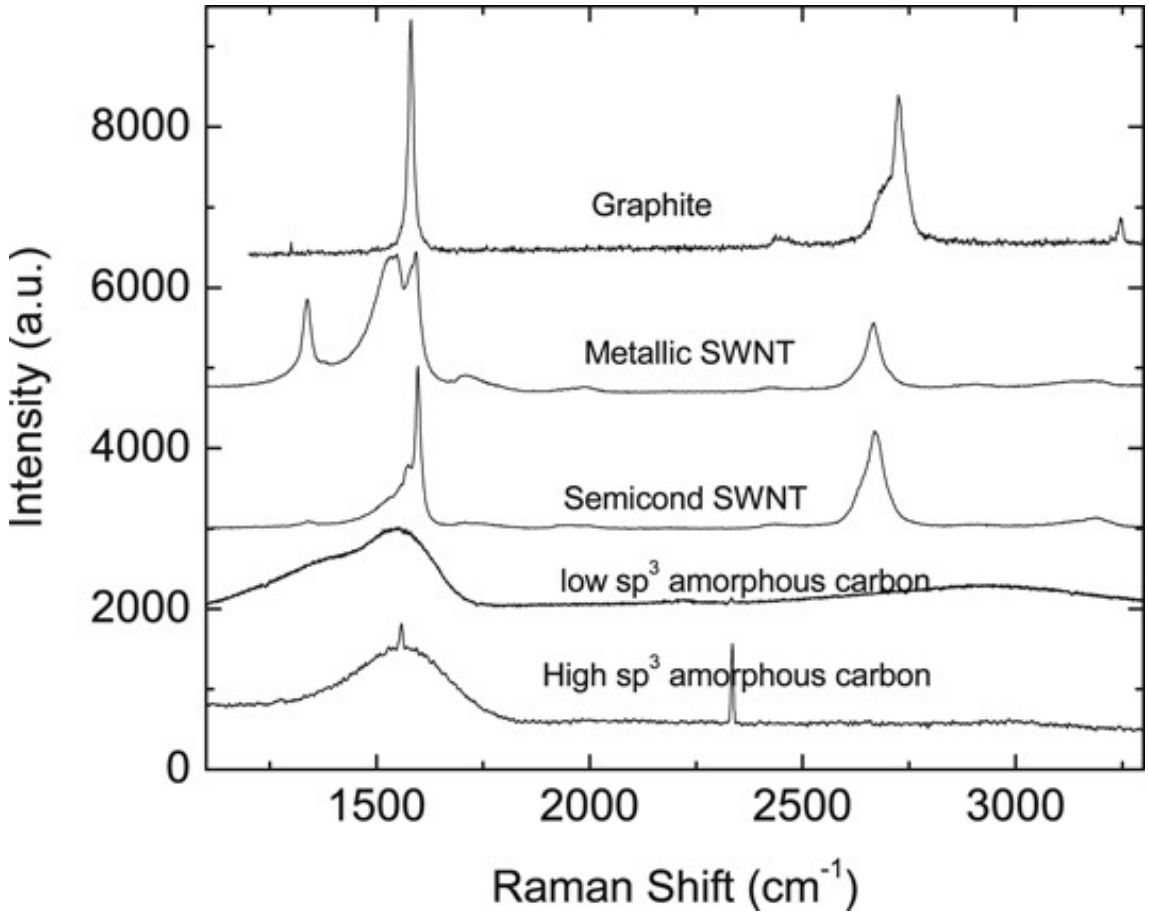

Figure 4-7 Raman spectra of graphite, metallic and semiconducting carbon nanotubes, low and high sp^3 amorphous carbons [140]

The D' peak (also called as 2D peak) occurs around 2700 cm^{-1}. The shape, the position and the intensity relative to the D peak of this peak depend on the number of layers of the sample.

4.5 Graphene as an electrode in Organic Solar Cells

Among other application areas, using graphene in organic photovoltaics interested researchers for the last couple of years [103, 142, 143]. Organic photovoltaics have a high potential and many advantages in the renewable energy area. The recent improvements in the device structure, fabrication techniques and new materials resulted a power conversion efficiency of 6%-7% under AM 1.5 G solar illumination [144]. The trend of the improvements shows that power conversion efficiency of organic photovoltaics can reach to the commercialization barrier of 10% in the next 10 years. Except the power conversion efficiency, the most important criterion for the commercialization is the device cost. Recent improvements in organic photovoltaics increase not only the power conversion efficiency but also the cost of the device.

In this case, the most reasonable solution to the high device cost is to replace the most expensive material in the device with a cheaper equivalent. In organic photovoltaics, most expensive part is the ITO electrode. Because it is not one of the earth's natural resources, indium is a rare material on the earth. But this rare material is used in many electronic applications such as LCD displays [145], organic photovoltaics [146], touch screens [147] because of its high mobility, low resistance (<100 ohms/sq.) and high transparent thin film characterization. (visible transmittance of >80%)

So, it is difficult to replace ITO thin films with another thin film. But, with the recent developments, graphene thin films can be an alternative to ITO thin films. In the

next chapter, we are going to show an application of large area graphene sheets in the organic photovoltaics as the transparent electrode.

4.6 Materials and Methods

CVD growth large area graphene can be used as an electrode in organic photovoltaics by adjusting its surface and electrical properties. First, transparency of the graphene films must be high enough for the light absorption. For this purpose large area graphene samples are grown with different number of layers.

For graphene fabrication, one inch by one inch size cupper fouls are placed in the MTI 1100 CVD furnace. First the chamber is annealed to 1000 °C for 15 minutes and a mixture of CH_4, H_2 and Ar gases are inserted with the flow rates of 500 sccm, 500 sccm and 250 sccm respectively.. The growth process takes from 10 to 20 minutes depending on the number of layers. After the growth, the samples are left 30 minutes for cooling [105]. Then the samples are taken into iron (iii) chloride ($FeCl_3$) solution (1 M) for overnight to dissolve the copper layers. At last, graphene flakes, which are flowing on the $FeCl_3$ solution, are taken onto a glass with the fishing method.

The transparency measurements are taken by the PerkinElmer Lambda 45 UV-VIS spectrometer. The range is chosen between 400 nm and 1100 nm. Four different samples are measured where the number of graphene layers is from one to four.

Another important criteria for the application of the graphene as the transparent electrode is the low surface resistance. Surface resistance measurements are taken Van der Pauw Method [148]. According to this method, four small contacts are fabricated on the four sides of the graphene sheet as shown in fig. Here, the ratio of the distance between the contacts to the contact size must be greater than 50. Then the voltage- current measurements are taken for two different cases. (Figure 4-8) Neglecting the thickness of sheet, the overall sheet resistance is found using this two resistance values as in the equation 4.1 [149, 150]. The unit of this resistance is Ω/□.

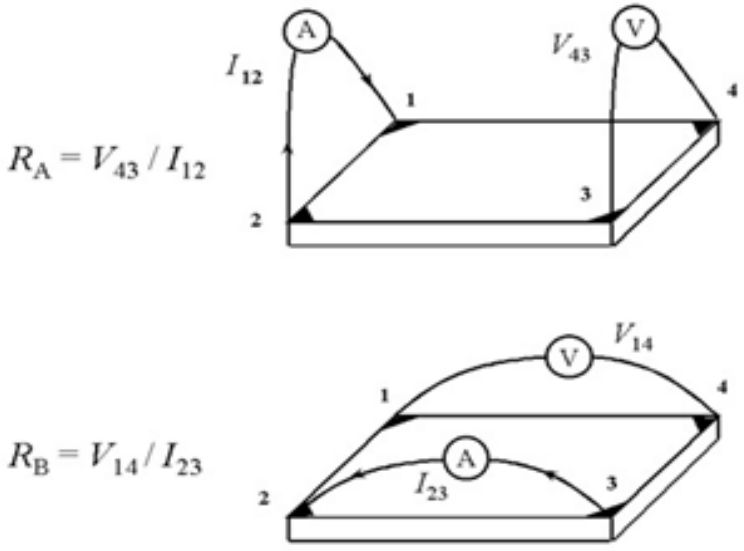

Figure 4-8 Explanation of the Van der Pauw method which is used in the sheet resistance calculations [148]

$$R_s = 4.5324 \frac{R_A + R_B}{2} \quad (4.1)$$

Surface wettability is also important for the graphene electrode applications. After the CVD fabrication, graphene is hydrophobic. To be applicable for the organic photovoltaics, surface properties must be changed to hydrophilic. Two different surface functionalization methods are applied to change the surface properties. (Figure 4-9) In one method, graphene surface is treated with a short duration of Ar plasma. By the help of the highly energized Ar molecules, some of the molecules in the graphene layer are removed. In another method, graphene surface is functionalized with HNO_3 molecules. The effects of these surface treatments over the surface wettability are examined by measuring the contact angle with Kruss EasyDrop Contact Angle Measuring system.

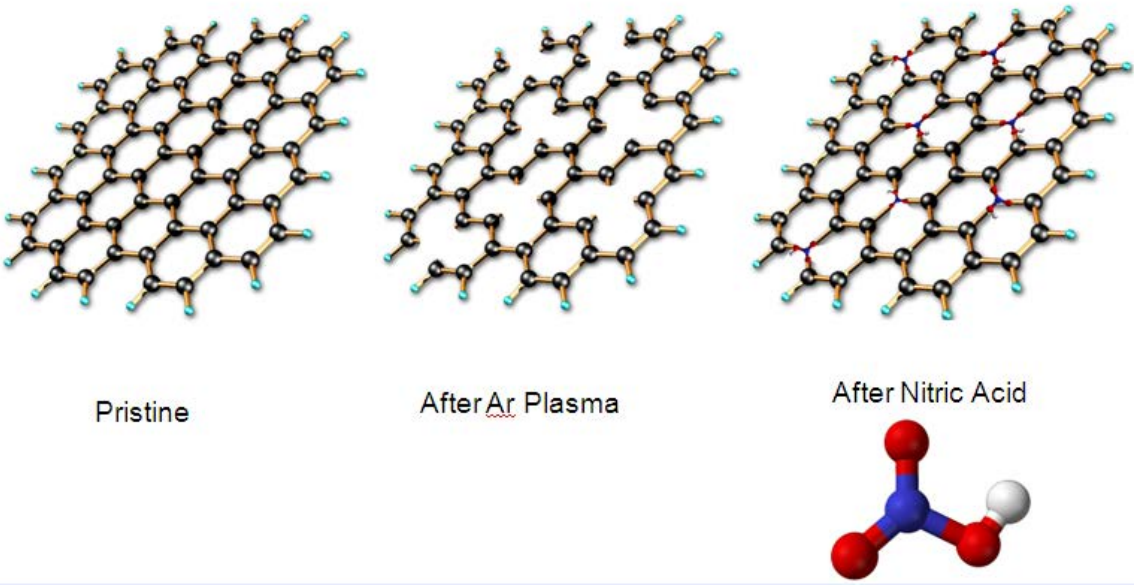

Figure 4-9 Two different methods of the surface functionalization to the pristine graphene material (Adapted from [151])

For the organic photovoltaic cell fabrication, ITO coated glasses (Delta Technologies 15 Ω/sq.) were ultrasonically cleaned with de-ionized water, acetone, isopropanol alcohol. Then the samples kept in a vacuum oven at 120℃ overnight. This process is followed by an air plasma treatment of 5min to remove the organic contaminants. Following the plasma treatment, a thin layer of PEDOT:PSS (Baytron P) was spin-coated from aqueous solution at 4000 rpm for 40 s, after passing through 0.45 μm syringe filter. The substrate was then baked at 150℃ for 15 minutes in air. Next, a mixture of 15mg (P3HT) and 15mg (PCBM) blend was dissolved in 1 ml (ODCB), and stirred for 12 hours at 70°C. After passing through a 0.2 μm filter, The P3HT/PCBM blend was deposited on top of the DNA or Pt-DNA layer at 700 rpm for 50 s via spin-coating. High temperature annealing treatment was carried in argon environment for 30 min at 120 ℃. The sample was then cooled back to room temperature within a 30 minute ramp. 1 nm thick LiF and 80 nm thick Al layers were subsequently evaporated through a shadow mask with 4mm x 4mm square openings.

For the graphene electrode applications, same fabrication procedure is applied onto the functionalized graphene substrate.

The characterization of the devices was done by using a Xe lamp by Newport Inc which simulates AM 1.5G light from 400 to 1100 nm and Agilent 4155 Semiconductor parameter analyzer. The IV data is then processed and device parameters are found in Matlab.

AFM imaging of the graphene films are performed on a Veeco Multimode V microscope in tapping mode.

4.7 Results and discussion

The CVD growth graphene films are characterized with two techniques. First, 1'x1' graphene sheets are fabricated for the AFM characterization. Then, the films are taken onto a pre-cleaned Si substrate. AFM images show that graphene films are uniformly grown. (Figure 4.10) The bright colors in the height image shows that the flake is cracked during the fishing process or there is a particle under the flake. But the cross section graph clearly shows that a 2nm thick (3-4 layers of graphene) graphene sheets are fabricated.

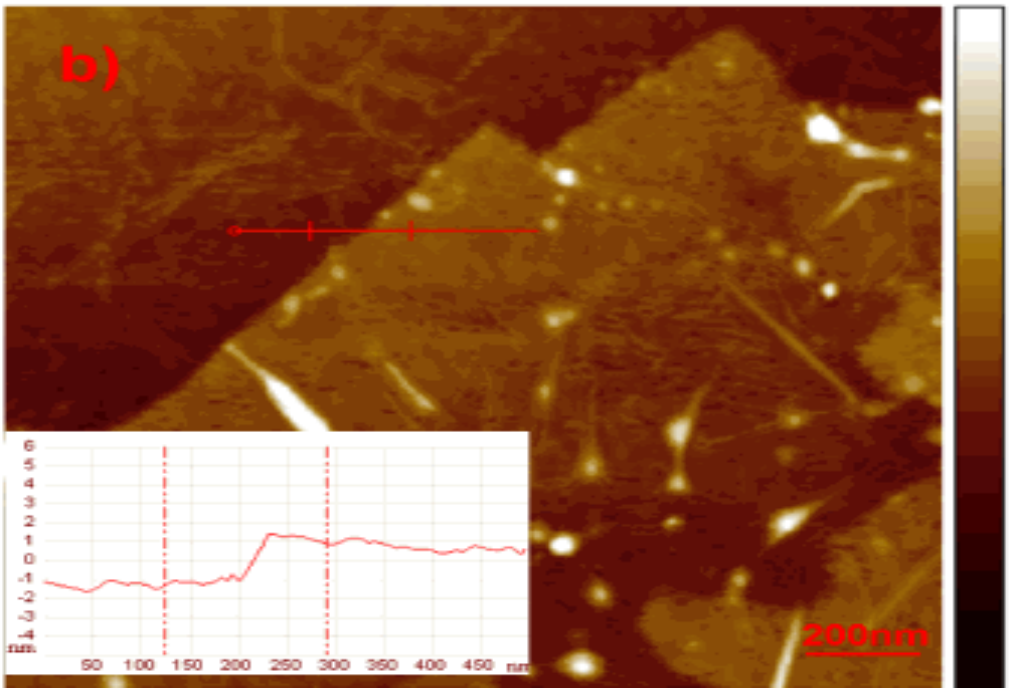

Figure 4-10 AFM height image of the CVD growth graphene

For a better understanding of the growth process and the graphene sheet quality, Raman spectroscopy is applied to the samples. (Figure 4-11) Here, the ratio of the G and 2D peaks determines the number of layers. As in the single layer graph, intensity of the 2D peak is more than double of the intensity of the G peak. In bi-layer graphene this ratio is around one. It is also important to notice that, both in single and bilayer graphene sheets, there is a significantly high D peak. This shows that there are some defects on the surface. These defects are mainly caused by the transfer process of graphene to the substrate. In the fishing method, graphene can easily crack or the flakes can fold onto each other. This results a significant increase in the surface resistance.

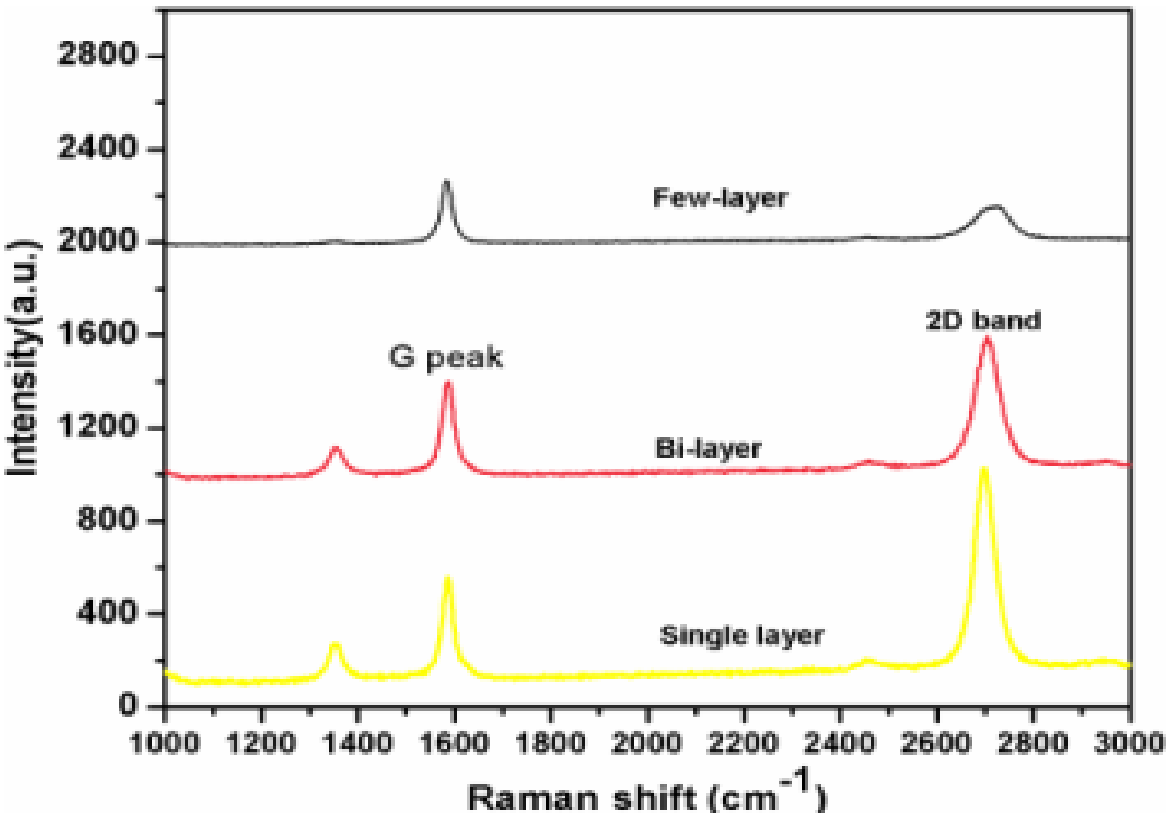

Figure 4-11 Raman Spectra of the single, bi and multi layer graphene

Another criterion for the electrode application of graphene sheets is the high transmittance. Since ITO coated glasses have a transmission rate of more than 80% over the visible and near IR range, similar properties are desired for the graphene too. (Figure 4-12) As the transmission spectra of one, two, three and four layers are taken, it is observed that each layer decreases the transmission by 2.5%. The results also show that even 4 layers of graphene has appropriate transmission rate for the organic photovoltaic devices.

It is also important to notice that as the number of layers increases, the transmission rate decreases faster in the near UV range than in the visible range. Because P3HT:PCBM based organic solar cells has an absorption spectra in the near UV range, using more than three layers of graphene as an electrode inhibits the absorption of the light spectrum in that range.

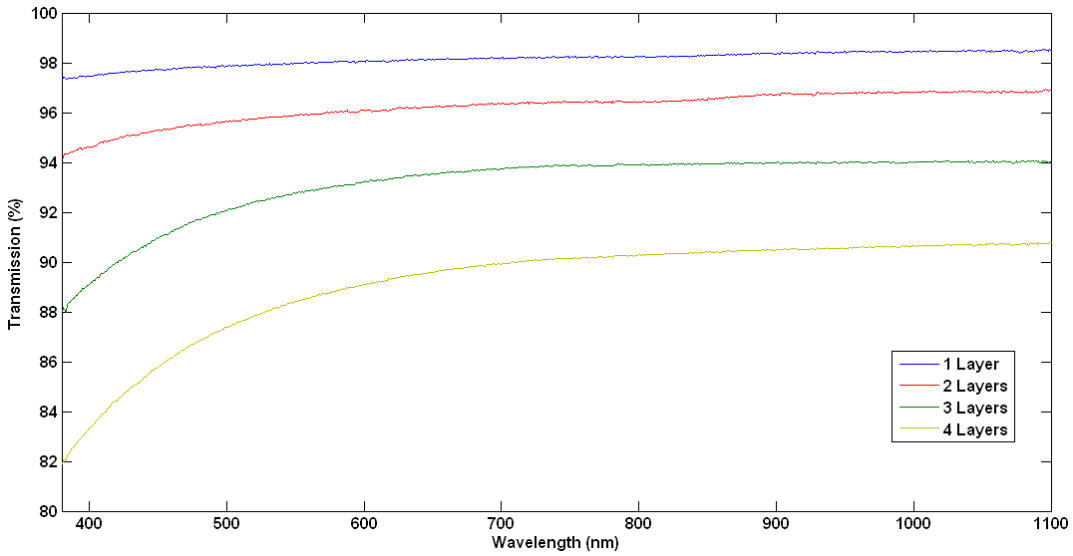

Figure 4-12 Transmission spectra of the one, two, three and four layers of large area graphene sheets

When the surface properties of the sheets are considered, two criteria are important; wettability and sheet resistance. Wettability is increased by two different surface treatments. As the surface becomes more hydrophilic, contact angle of the DI water droplet is decreased. First 5 sec. of Ar plasma is applied to the surface. After the Ar plasma, surface wettability increased significantly. (Figure 4-13)

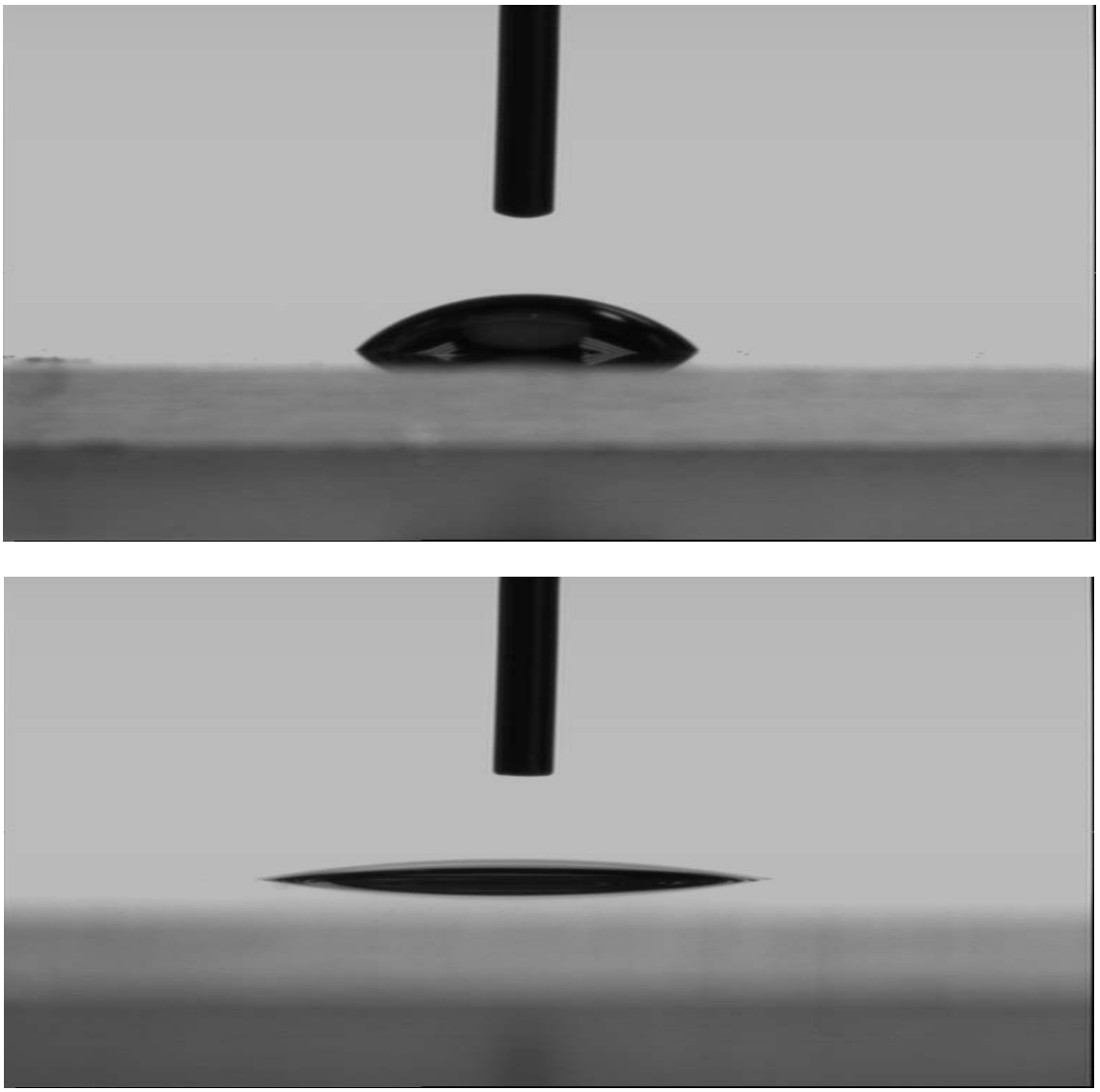

Figure 4-13 Bi-layer of Graphene before and after Argon plasma

As in Table 4-1, increasing the number of layers decreases the contact angle. Increasing the number of layers from one to three decreases the contact angle by 17%. However, without any treatment, pristine graphine shows hydrophobic characteristics. When Ar plasma is applied to the surface, the contact angles in all cases decreases by 50% or higher. This shows that after Ar plasma, graphene surface becomes highly hydrophilic. However, it is observed that while it is increasing the wettability of the surface, Ar plasma does not improve over the sheet resistance.

To decrease the sheet resistance, surface is functionalized with nitric acid. The effect of this treatment over the surface wettability is also investigated. According to the results, contact angle increases by 10° in all cases.

Table 4-1 Contact angle measurements for single, bi and multi layer graphene samples before and after surface treatments

# of Graphene Layers	Pristine (°)	After Argon Plasma (°)	After functionalization (°)
1	57.96	26.22	43.27
2	50.76	19.3	27.74
3	48.01	22.6	33.64
4	48.48	25.84	34.68

The effects of the surface treatments over the surface resistance are also investigated in Table 4-2. Different from the contact angle measurements, there is an intermediate step is also investigated by annealing the samples at 300°C. Annealing is

expected to clean the surface and remove the O_2 from the oxided graphene. According to the results, annealing slightly increases the resistance of single layer graphene by 6%. This can be explained by removing the particles and O_2 from the single layer graphene, increases the number of defects over the surface. However, in three layer graphene case, annealing decreases the surface resistance by 20%.

Further treatments of Ar plasma to the single layer graphene easily destroy the layer formation of the graphene sheets. However, when it is used in multilayer graphene sheets, it slightly increases the sheet resistance. The tradeoff this increase is the decrease in the surface wettability.

To decrease the sheet resistance further, nitric acid treatment is applied. The results show that this treatment overcomes the losses caused by the Ar plasma. As a result of these treatment processes, the surface resistance of the three layers of graphene is decreased by 25%.

Table 4-2 Effects of the surface treatment over the sheet resistance of single and three layers of graphene

# of Layers	Pristine	After annealing at 300°C	After Argon Plasma	After Func.
1 layer Graphene	1.6 KΩ/sq.	1.7 KΩ/sq.	---	--
3 layers of Graphene	992 Ω/sq.	792 Ω/sq.	856 Ω/sq.	724 Ω/sq.

After the surface treatments, ITO and graphene sheets are used for organic solar cell fabrication. As can be seen from Table 4-3, open circuit voltage in both cases remains close because the open circuit voltage is mainly determined by the energy levels of the active layer polymers. But, current density of the graphene solar cell is significantly lower than the one of the ITO. This is mainly caused by the high sheet resistance of the graphene substrate. The high resistance increases the series resistance of the device and leads to a decrease in the current density. As a result, power conversion efficiency is significantly lower than the ITO based solar cells.

Table 4-3 Organic solar cell parameters for ITO and graphene anode contact devices

Device	V_{oc} (V)	J_{sc} (mA/cm^2)	FF	η (%)
ITO	0.6	15	38	3.5
Graphene	0.56	3.31	22	.42

4.8 Conclusion

In conclusion, graphene is used as an anode electrode in organic photovoltaic devices. The results show that without any treatment, graphene cannot be used as a transparent electrode. However, some basic surface treatments show a significant increase in the surface and the electrical properties of the graphene sheets. Moreover, it is shown that maximum of three layers of graphene can be used for higher light absorption of the

active layer polymers in the UV region. Although graphene sheets show promising results in transmission and surface wettability after the Ar plasma and Nitric acid treatments, high surface resistance remains the main issue for the graphene electrodes. As a result, graphene has a potential to replace the ITO but further improvements in the device fabrication and surface functionalization are required.

Chapter 5:

Conclusions

In conclusion, two approaches were successfully developed and applied to increase the device performance of the organic solar cells and to decrease the device cost. It was demonstrated that, by using DNA in the hole collection side of the organic solar devices, hole collection ability is enhanced. Moreover, it was shown that by optimizing the metallization process of DNA strands, 1-D quasi-metallic nanostructures can be fabricated. When these metalized DNA nanostructures used in organic solar cells, hole collection is enhanced more. When the reasons of these improvements are investigated, it is observed that by having negatively charged characteristics, DNA introduces alternative desirable pathways to the holes and metallization of DNA decreases the resistance of this pathways. These achievements show the potential of DNA and DNA template nanowires in organic photovoltaics.

In this dissertation, the cost of the organic solar cell is tried to reduce by replacing the anode contact with large area graphene thin films. Single and multi layer graphene thin films are developed in CVD furnaces and they are optically and electrically characterized. The results show that they have similar optical properties with ITO thin films but their electrical properties are comparably lower than ITO. Two different approached are studied to enhance the electrical properties. As a result, the device performance results are found

as comparably lower than ITO device performance. However, the improvements we found show that graphene is the best candidate to replace the ITO.

Chapter 6:

References

[1] BP statistical review - NG World energy 2007. Int Gas Eng Manag. 2008;48(1):8-12.

[2] Würfel P. Physics of solar cells : from principles to new concepts. Weinheim: Wiley-VCH; 2005.

[3] Hatfield CB. Oil back on the global agenda. Nature. 1997;387(6629):121-.

[4] Energy usage of world. [cited 2010; Past, recent and expected future energy usage of world in crude oil equivalents between 1971 and 2030]. Available from: http://www.enecho.meti.go.jp/en/

[5] World Energy Assesment Report: Energy and Challenge of Sustainability. United Nations, New York; 2003.

[6] Chapin DM, Fuller CS, Pearson GL. A New Silicon P-N Junction Photocell for Converting Solar Radiation into Electrical Power. J Appl Phys. 1954;25(5):676-7.

[7] Green MA. Third generation photovoltaics: solar cells for 2020 and beyond. Physica E. 2002;14(1-2):65-70.

[8] Sun S-S, Sariciftci NS. Organic photovoltaics : mechanisms, materials, and devices. Boca Raton, FL: Taylor & Francis; 2005.

[9] Keavney CJ, Spitzer MB. INDIUM-PHOSPHIDE SOLAR-CELLS MADE BY ION-IMPLANTATION. Applied Physics Letters. 1988;52(17):1439-40.

[10] Carlson DE, Wronski CR. AMORPHOUS SILICON SOLAR-CELL. Applied Physics Letters. 1976;28(11):671-3.

[11] Ohtake Y, Kushiya K, Ichikawa M, Yamada A, Konagai M. Polycrystalline Cu(InGa)Se-2 thin-film solar cells with ZnSe buffer layers. Jpn J Appl Phys Part 1 - Regul Pap Short Notes Rev Pap. 1995;34(11):5949-55.

[12] Dobson KD, Visoly-Fisher I, Hodes G, Cahen D. Stability of CdTe/CdS thin-film solar cells. Sol Energ Mat Sol C. 2000;62(3):295-325.

[13] Kazmersk L. Best research solar cells efficiencies. [cited 2010; Chart of the highest research cell efficiencies between 1975 and 2010]. Available from: http://www.nrel.gov/ncpv/

[14] Li G, Shrotriya V, Huang JS, Yao Y, Moriarty T, Emery K, et al. High-efficiency solution processable polymer photovoltaic cells by self-organization of polymer blends. Nat Mater. 2005;4(11):864-8.

[15] Green MA, Emery K, King DL, Hisikawa Y, Warta W. Solar cell efficiency tables (Version 27). Prog Photovoltaics. 2006;14(1):45-51.

[16] Solar Spectrum. [cited 2010; The solar radiation spectrum for direct light at both the top of the Earth's atmosphere and at sea level]. Available from: http://en.wikipedia.org/wiki/Greenhouse_effect

[17] Chiang CK, Fincher CR, Park YW, Heeger AJ, Shirakawa H, Louis EJ, et al. Electrical-Conductivity in Doped Polyacetylene. Phys Rev Lett. 1977;39(17):1098-101.

[18] Burroughes JH, Bradley DDC, Brown AR, Marks RN, Mackay K, Friend RH, et al. Light-Emitting-Diodes Based on Conjugated Polymers. Nature. 1990;347(6293):539-41.

[19] Friend RH, Gymer RW, Holmes AB, Burroughes JH, Marks RN, Taliani C, et al. Electroluminescence in conjugated polymers. Nature. 1999;397(6715):121-8.
[20] Sariciftci NS, Braun D, Zhang C, Srdanov VI, Heeger AJ, Stucky G, et al. Semiconducting Polymer-Buckminsterfullerene Heterojunctions - Diodes, Photodiodes, and Photovoltaic Cells. Applied Physics Letters. 1993;62(6):585-7.
[21] Yu G, Gao J, Hummelen JC, Wudl F, Heeger AJ. Polymer Photovoltaic Cells - Enhanced Efficiencies Via a Network of Internal Donor-Acceptor Heterojunctions. Science. 1995;270(5243):1789-91.
[22] Hoffmann R, Janiak C, Kollmar C. A Chemical Approach to the Orbitals of Organic Polymers. Macromolecules. 1991;24(13):3725-46.
[23] Polyacetylene. [cited 2010; Structural diagram of Polyacetylene]. Available from: http://www.nobelprize.org/nobel_prizes/chemistry/laureates/2000/popular.html
[24] Homo-Lumo Gap. [cited 2010; Changes in the electron energy levels of a conjugated polymer before and after the photon absorption]. Available from: http://www.chem.ucla.edu/harding/IGOC/H/homo_lumo_gap.html
[25] Kietzke T. Recent Advances in Organic Solar Cells. Advances in OptoElectronics. 2007;2007:15.
[26] McGhee MD, Topinka MA. Solar cells: Pictures from the blended zone. Nat Mater. 2006;5(9):675-6.
[27] Granstrom M, Petritsch K, Arias AC, Lux A, Andersson MR, Friend RH. Laminated fabrication of polymeric photovoltaic diodes. Nature. 1998;395(6699):257-60.
[28] Shaheen SE, Brabec CJ, Sariciftci NS, Padinger F, Fromherz T, Hummelen JC. 2.5% efficient organic plastic solar cells. Appl Phys Lett. 2001;78(6):841-3.
[29] Schilinsky P, Waldauf C, Brabec CJ. Recombination and loss analysis in polythiophene based bulk heterojunction photodetectors. Applied Physics Letters. 2002;81(20):3885-7.
[30] Padinger F, Rittberger RS, Sariciftci NS. Effects of postproduction treatment on plastic solar cells. Adv Funct Mater. 2003;13(1):85-8.
[31] Liang YY, Xu Z, Xia JB, Tsai ST, Wu Y, Li G, et al. For the Bright Future-Bulk Heterojunction Polymer Solar Cells with Power Conversion Efficiency of 7.4%. Advanced Materials. 2010;22(20):E135-+.
[32] Steckl AJ. DNA - a new material for photonics? Nature Photonics. 2007;1(1):3-5.
[33] Phenyl-C61-butyric acid methyl ester. [cited 2010; Structure of Phenyl-C61-butyric acid methyl ester]. Available from: http://en.wikipedia.org/wiki/Phenyl-C61-butyric_acid_methyl_ester
[34] Dennler G, Lungenschmied C, Neugebauer H, Sariciftci NS, Labouret A. Flexible, conjugated polymer-fullerene-based bulk-heterojunction solar cells: Basics, encapsulation, and integration. J Mater Res. 2005;20(12):3224-33.
[35] Kim JY, Kim SH, Lee HH, Lee K, Ma WL, Gong X, et al. New architecture for high-efficiency polymer photovoltaic cells using solution-based titanium oxide as an optical spacer. Advanced Materials. 2006;18(5):572-+.
[36] Fox M. Optical properties of solids. Oxford ; New York: Oxford University Press; 2001.
[37] Gaudin OPM, Samuel IDW, Amriou S, Burn PL. Thickness dependent absorption spectra in conjugated polymers: Morphology or interference? Applied Physics Letters. 2010;96(5):-.

[38] van Bavel S, Sourty E, de With G, Frolic K, Loos J. Relation between Photoactive Layer Thickness, 3D Morphology, and Device Performance in P3HT/PCBM Bulk-Heterojunction Solar Cells. Macromolecules. 2009;42(19):7396-403.
[39] Shrotriya V, Li G, Yao Y, Moriarty T, Emery K, Yang Y. Accurate measurement and characterization of organic solar cells. Adv Funct Mater. 2006;16(15):2016-23.
[40] Quantum Efficiency. [cited 2010; Definition of incident photon to converted electron efficiency (IPCE) and internal quantum efficiency (IQE)]. Available from: http://en.wikipedia.org/wiki/Quantum_efficiency
[41] The equivalent circuit of a solar cell. [cited 2010; Simplified Equivalent Circuit Model for a Photovoltaic Cell]. Available from: http://en.wikipedia.org/wiki/Theory_of_solar_cells
[42] Kumar P, Jain SC, Kumar V, Chand S, Tandon RP. A model for the J-V characteristics of P3HT:PCBM solar cells. J Appl Phys. 2009;105(10).
[43] Current-Voltage Characteristics of Organic Solar Cells. [cited 2010; Current-voltage (I-V) curves of an organic solar cell under dark and illumination]. Available from: http://blog.disorderedmatter.eu/2008/03/05/intermediate-current-voltage-characeristics-of-organic-solar-cells/
[44] Brabec CJ, Cravino A, Meissner D, Sariciftci NS, Fromherz T, Rispens MT, et al. Origin of the open circuit voltage of plastic solar cells. Advanced Functional Materials. 2001;11(5):374-80.
[45] Scharber MC, Wuhlbacher D, Koppe M, Denk P, Waldauf C, Heeger AJ, et al. Design rules for donors in bulk-heterojunction solar cells - Towards 10 % energy-conversion efficiency. Advanced Materials. 2006;18(6):789-+.
[46] Kroon R, Lenes M, Hummelen JC, Blom PWM, De Boer B. Small bandgap polymers for organic solar cells (polymer material development in the last 5 years). Polym Rev. 2008;48(3):531-82.
[47] Goetzberger A, Knobloch J, Voss B. Crystalline silicon solar cells. Chichester ; New York: Wiley; 1998.
[48] Short circuit current of a solar cell [cited 2010; The elements generating the current of the solar cell]. Available from: http://quanta.hanyang.ac.kr/Education/Education_Solar_CE.htm
[49] Dennler G, Sariciftci NS. Flexible conjugated polymer-based plastic solar cells: From basics to applications. Proceedings of the Ieee. 2005;93(8):1429-39.
[50] Rostalski J, Meissner D. Photocurrent spectroscopy for the investigation of charge carrier generation and transport mechanisms in organic p/n-junction solar cells. Sol Energ Mat Sol C. 2000;63(1):37-47.
[51] Wohrle D, Meissner D. Organic Solar-Cells. Advanced Materials. 1991;3(3):129-38.
[52] Brabec CJ, Hauch JA, Schilinsky P, Waldauf C. Production aspects of organic photovoltaics and their impact on the commercialization of devices. Mrs Bulletin. 2005;30(1):50-2.
[53] Haugeneder A, Neges M, Kallinger C, Spirkl W, Lemmer U, Feldmann J, et al. Exciton diffusion and dissociation in conjugated polymer fullerene blends and heterostructures. Physical Review B. 1999;59(23):15346-51.
[54] Morana M, Wegscheider M, Bonanni A, Kopidakis N, Shaheen S, Scharber M, et al. Bipolar charge transport in PCPDTBT-PCBM bulk-heterojunctions for photovoltaic applications. Advanced Functional Materials. 2008;18(12):1757-66.
[55] Kannan B, Castelino K, Majumdar A. Design of nanostructured heterojunction polymer photovoltaic devices. Nano Lett. 2003;3(12):1729-33.

[56] Kymakis E, Kornilios N, Koudoumas E. Carbon nanotube doping of P3HT: PCBM photovoltaic devices. J Phys D Appl Phys. 2008;41(16):-.
[57] Huynh WU, Dittmer JJ, Alivisatos AP. Hybrid nanorod-polymer solar cells. Science. 2002;295(5564):2425-7.
[58] Arici E, Sariciftci NS, Meissner D. Hybrid solar cells based on nanoparticles of CuInS2 in organic matrices. Advanced Functional Materials. 2003;13(2):165-71.
[59] Xin H, Kim FS, Jenekhe SA. Highly efficient solar cells based on poly(3-butylthiophene) nanowires. Journal of the American Chemical Society. 2008;130(16):5424-+.
[60] Hashimoto Y, Hamagaki M. Effect of oxygen plasma treatment of indium tin oxide for organic solar cell. Electr Eng Jpn. 2006;154(4):1-7.
[61] Brabec CJ, Shaheen SE, Winder C, Sariciftci NS, Denk P. Effect of LiF/metal electrodes on the performance of plastic solar cells. Applied Physics Letters. 2002;80(7):1288-90.
[62] Wang X, Pandey RR, Singh KV, Andavan GTS, Tsai C, Lake R, et al. Synthesis and characterization of peptide nucleic acid-platinum nanoclusters. Nanotechnology. 2006;17(5):1177-83.
[63] Chaudhary S, Lu HW, Muller AM, Bardeen CJ, Ozkan M. Hierarchical placement and associated optoelectronic impact of carbon nanotubes in polymer-fullerene solar cells. Nano Lett. 2007;7(7):1973-9.
[64] Chaudhary S, Kim JH, Singh KV, Ozkan M. Fluorescence microscopy visualization of single-walled carbon nanotubes using semiconductor nanocrystals. Nano Lett. 2004;4(12):2415-9.
[65] Schaeffer JK, Fonseca LRC, Samavedam SB, Liang Y, Tobin PJ, White BE. Contributions to the effective work function of platinum on hafnium dioxide. Applied Physics Letters. 2004;85(10):1826-8.
[66] Kim Y, Choi D, Moon B, Oh E, Lim H, Kwon S, et al. Controllable work function of Li-Al alloy nanolayers for organic light-emitting devices. Advanced Engineering Materials. 2005;7(11):1023-7.
[67] Yengel EW, L.; Ozkan, M.; Ozkan, C. S. Effects of DNA and Pt-DNA electrodes on bulk heterojuction solar cells. Nanoscale Photonic and Cell Technologies for Photovoltaics II. San Diego: SPIE Proceedings 2009, p. 74110B-B-6.
[68] Kwon YW, Lee CH, Choi DH, Jin JI. Materials science of DNA. J Mater Chem. 2009;19(10):1353-80.
[69] Benedetti M, Ducani C, Migoni D, Antonucci D, Vecchio VM, Romano A, et al. Possible Incorporation of Free N7-Platinated Guanines in DNA by DNA Polymerases, Relevance for the Cisplatin Mechanism of Action: Humana Press Inc; 2009.
[70] Miller AJ, Hatton RA, Silva SRP. Interpenetrating multiwall carbon nanotube electrodes for organic solar cells. Applied Physics Letters. 2006;89(13):-.
[71] Jain A, Kapoor A. A new approach to study organic solar cell using Lambert W-function. Solar Energy Materials and Solar Cells. 2005;86(2):197-205.
[72] Singh VN, Singh RP. A Method for the Measurement of Solar-Cell Series Resistance. J Phys D Appl Phys. 1983;16(10):1823-5.
[73] Mertig M, Ciacchi LC, Seidel R, Pompe W, De Vita A. DNA as a selective metallization template. Nano Lett. 2002;2(8):841-4.
[74] Seidel R, Ciacchi LC, Weigel M, Pompe W, Mertig M. Synthesis of platinum cluster chains on DNA templates: Conditions for a template-controlled cluster growth. J Phys Chem B. 2004;108(30):10801-11.

[75] Wang X, Liu F, Wang KL, Ozkan CS. Metallized DNA nanotemplates for the fabrication of ZnO nanostructures for optoelectronic applications. Journal of Nanoelectronics and Optoelectronics. 2006;1(2):203-10.
[76] Seidel R, Mertig M, Pompe W. Scanning force microscopy of DNA metallization. Surface and Interface Analysis. 2002;33(2):151-4.
[77] Richter J, Seidel R, Kirsch R, Mertig M, Pompe W, Plaschke J, et al. Nanoscale palladium metallization of DNA. Advanced Materials. 2000;12(7):507-+.
[78] Deng ZX, Mao CD. DNA-templated fabrication of 1D parallel and 2D crossed metallic nanowire arrays. Nano Lett. 2003;3(11):1545-8.
[79] Pierret RF. Field effect devices. Reading, MA: Addison-Wesley; 1983.
[80] Na M, Rhee SW. Electronic characterization of Al/PMMA[poly(methyl methacrylate)]/p-Si and Al/CEP(cyanoethyl pullulan)/p-Si structures. Org Electron. 2006;7(4):205-12.
[81] Matocha K, Chow TP, Gutmann RJ. Positive flatband voltage shift in MOS capacitors on n-type GaN. Ieee Electron Device Letters. 2002;23(2):79-81.
[82] Soldano C, Mahmood A, Dujardin E. Production, properties and potential of graphene. Carbon. 2010;48(8):2127-50.
[83] Novoselov KS, Geim AK, Morozov SV, Jiang D, Katsnelson MI, Grigorieva IV, et al. Two-dimensional gas of massless Dirac fermions in graphene. Nature. 2005;438(7065):197-200.
[84] Zhang YB, Tan YW, Stormer HL, Kim P. Experimental observation of the quantum Hall effect and Berry's phase in graphene. Nature. 2005;438(7065):201-4.
[85] Morozov SV, Novoselov KS, Katsnelson MI, Schedin F, Elias DC, Jaszczak JA, et al. Giant intrinsic carrier mobilities in graphene and its bilayer. Phys Rev Lett. 2008;100(1):-.
[86] Bolotin KI, Sikes KJ, Jiang Z, Klima M, Fudenberg G, Hone J, et al. Ultrahigh electron mobility in suspended graphene. Solid State Commun. 2008;146(9-10):351-5.
[87] Bolotin KI, Sikes KJ, Hone J, Stormer HL, Kim P. Temperature-dependent transport in suspended graphene. Phys Rev Lett. 2008;101(9):-.
[88] Du X, Skachko I, Barker A, Andrei EY. Approaching ballistic transport in suspended graphene. Nat Nanotechnol. 2008;3(8):491-5.
[89] Zhang Y, Jiang Z, Small JP, Purewal MS, Tan YW, Fazlollahi M, et al. Landau-level splitting in graphene in high magnetic fields. Phys Rev Lett. 2006;96(13):-.
[90] Geim AK, Novoselov KS. The rise of graphene. Nat Mater. 2007;6(3):183-91.
[91] Ozyilmaz B, Jarillo-Herrero P, Efetov D, Abanin DA, Levitov LS, Kim P. Electronic transport and quantum hall effect in bipolar graphene p-n-p junctions. Phys Rev Lett. 2007;99(16):-.
[92] Novoselov K. Mind the gap. Nat Mater. 2007;6(10):720-1.
[93] Areshkin D. Graphene simulations hint at future electronics. Nanotechweb. http://nanotechweb.org/cws/article/indepth/31360 2007.
[94] Shemella P, Zhang Y, Mailman M, Ajayan PM, Nayak SK. Energy gaps in zero-dimensional graphene nanoribbons. Applied Physics Letters. 2007;91(4):-.
[95] Wakabayashi K, Takane Y, Yamamoto M, Sigrist M. Electronic transport properties of graphene nanoribbons. New J Phys. 2009;11:-.
[96] Li D, Muller MB, Gilje S, Kaner RB, Wallace GG. Processable aqueous dispersions of graphene nanosheets. Nat Nanotechnol. 2008;3(2):101-5.
[97] Eda G, Fanchini G, Chhowalla M. Large-area ultrathin films of reduced graphene oxide as a transparent and flexible electronic material. Nat Nanotechnol. 2008;3(5):270-4.

[98] Lee C, Wei XD, Kysar JW, Hone J. Measurement of the elastic properties and intrinsic strength of monolayer graphene. Science. 2008;321(5887):385-8.
[99] Bunch JS, Verbridge SS, Alden JS, van der Zande AM, Parpia JM, Craighead HG, et al. Impermeable atomic membranes from graphene sheets. Nano Letters. 2008;8(8):2458-62.
[100] Gilje S, Han S, Wang M, Wang KL, Kaner RB. A chemical route to graphene for device applications. Nano Letters. 2007;7(11):3394-8.
[101] Nagashima A, Itoh H, Ichinokawa T, Oshima C, Otani S. Change in the Electronic States of Graphite Overlayers Depending on Thickness. Phys Rev B. 1994;50(7):4756-63.
[102] Blake P, Brimicombe PD, Nair RR, Booth TJ, Jiang D, Schedin F, et al. Graphene-based liquid crystal device. Nano Letters. 2008;8(6):1704-8.
[103] Wang X, Zhi LJ, Mullen K. Transparent, conductive graphene electrodes for dye-sensitized solar cells. Nano Letters. 2008;8(1):323-7.
[104] Nair RR, Blake P, Grigorenko AN, Novoselov KS, Booth TJ, Stauber T, et al. Fine structure constant defines visual transparency of graphene. Science. 2008;320(5881):1308-.
[105] Reina A, Jia XT, Ho J, Nezich D, Son HB, Bulovic V, et al. Large Area, Few-Layer Graphene Films on Arbitrary Substrates by Chemical Vapor Deposition. Nano Letters. 2009;9(1):30-5.
[106] Lu XK, Yu MF, Huang H, Ruoff RS. Tailoring graphite with the goal of achieving single sheets. Nanotechnology. 1999;10(3):269-72.
[107] Zhang YB, Small JP, Pontius WV, Kim P. Fabrication and electric-field-dependent transport measurements of mesoscopic graphite devices. Applied Physics Letters. 2005;86(7):-.
[108] Novoselov KS, Geim AK, Morozov SV, Jiang D, Zhang Y, Dubonos SV, et al. Electric field effect in atomically thin carbon films. Science. 2004;306(5296):666-9.
[109] Blake P, Hill EW, Neto AHC, Novoselov KS, Jiang D, Yang R, et al. Making graphene visible. Applied Physics Letters. 2007;91(6):-.
[110] Stankovich S, Dikin DA, Dommett GHB, Kohlhaas KM, Zimney EJ, Stach EA, et al. Graphene-based composite materials. Nature. 2006;442(7100):282-6.
[111] Stankovich S, Dikin DA, Piner RD, Kohlhaas KA, Kleinhammes A, Jia Y, et al. Synthesis of graphene-based nanosheets via chemical reduction of exfoliated graphite oxide. Carbon. 2007;45(7):1558-65.
[112] Jung I, Pelton M, Piner R, Dikin DA, Stankovich S, Watcharotone S, et al. Simple approach for high-contrast optical imaging and characterization of graphene-based sheets. Nano Letters. 2007;7(12):3569-75.
[113] Yang D, Velamakanni A, Bozoklu G, Park S, Stoller M, Piner RD, et al. Chemical analysis of graphene oxide films after heat and chemical treatments by X-ray photoelectron and Micro-Raman spectroscopy. Carbon. 2009;47(1):145-52.
[114] Boehm HP, Clauss A, Fischer GO, Hofmann U. Das Adsorptionsverhalten Sehr Dunner Kohlenstoff-Folien. Z Anorg Allg Chem. 1962;316(3-4):119-27.
[115] Schniepp HC, Li JL, McAllister MJ, Sai H, Herrera-Alonso M, Adamson DH, et al. Functionalized single graphene sheets derived from splitting graphite oxide. J Phys Chem B. 2006;110(17):8535-9.
[116] McAllister MJ, Li JL, Adamson DH, Schniepp HC, Abdala AA, Liu J, et al. Single sheet functionalized graphene by oxidation and thermal expansion of graphite. Chem Mater. 2007;19(18):4396-404.
[117] Berger C, Song ZM, Li XB, Wu XS, Brown N, Naud C, et al. Electronic confinement and coherence in patterned epitaxial graphene. Science. 2006;312(5777):1191-6.

[118] de Heer WA, Berger C, Wu XS, First PN, Conrad EH, Li XB, et al. Epitaxial graphene. Solid State Commun. 2007;143(1-2):92-100.
[119] Kedzierski J, Hsu PL, Healey P, Wyatt PW, Keast CL, Sprinkle M, et al. Epitaxial graphene transistors on SIC substrates. Ieee T Electron Dev. 2008;55(8):2078-85.
[120] Allen MJ, Tung VC, Kaner RB. Honeycomb Carbon: A Review of Graphene. Chem Rev. 2010;110(1):132-45.
[121] Lemme MC, Echtermeyer TJ, Baus M, Kurz H. A graphene field-effect device. Ieee Electr Device L. 2007;28(4):282-4.
[122] Wu YQ, Ye PD, Capano MA, Xuan Y, Sui Y, Qi M, et al. Top-gated graphene field-effect-transistors formed by decomposition of SIC. Applied Physics Letters. 2008;92(8):-.
[123] Sutter PW, Flege JI, Sutter EA. Epitaxial graphene on ruthenium. Nat Mater. 2008;7(5):406-11.
[124] Gall' NR, Rut'kov EV, Tontegode AY. Interaction of silver atoms with iridium and with a two-dimensional graphite film on iridium: Adsorption, desorption, and dissolution. Phys Solid State+. 2004;46(2):371-7.
[125] Coraux J, N'Diaye AT, Busse C, Michely T. Structural coherency of graphene on Ir(111). Nano Letters. 2008;8(2):565-70.
[126] Vaari J, Lahtinen J, Hautojarvi P. The adsorption and decomposition of acetylene on clean and K-covered Co(0001). Catal Lett. 1997;44(1-2):43-9.
[127] de Parga ALV, Calleja F, Borca B, Passeggi MCG, Hinarejos JJ, Guinea F, et al. Periodically rippled graphene: Growth and spatially resolved electronic structure. Phys Rev Lett. 2008;100(5):-.
[128] Marchini S, Gunther S, Wintterlin J. Scanning tunneling microscopy of graphene on Ru(0001). Phys Rev B. 2007;76(7):-.
[129] Madden HH, Kuppers J, Ertl G. Interaction of Carbon-Monoxide with (110) Nickel Surfaces. J Chem Phys. 1973;58(8):3401-10.
[130] Starodubov AG, Medvetskii MA, Shikin AM, Adamchuk VK. Intercalation of silver atoms under a graphite monolayer on Ni(111). Phys Solid State+. 2004;46(7):1340-8.
[131] Kawano T, Kawaguchi M, Okamoto Y, Enomoto H, Bando H. Preparation of layered B/C/N thin films on nickel single crystal by LPCVD. Solid State Sci. 2002;4(11-12):1521-7.
[132] Ueta H, Saida M, Nakai C, Yamada Y, Sasaki M, Yamamoto S. Highly oriented monolayer graphite formation on Pt(111) by a supersonic methane beam. Surf Sci. 2004;560(1-3):183-90.
[133] Li XS, Cai WW, An JH, Kim S, Nah J, Yang DX, et al. Large-Area Synthesis of High-Quality and Uniform Graphene Films on Copper Foils. Science. 2009;324(5932):1312-4.
[134] Geim AK. Graphene: Status and Prospects. Science. 2009;324(5934):1530-4.
[135] Kumar S, McEvoy N, Lutz T, Keeley G, Duesberg G. Heteroepitaxial CVD growth of Graphene. Intel European Research and Innovation Conference. School of Chemistry, Trinity College, Dublin.
[136] Li L, Liu RP, Chen ZW, Wang Q, Ma MZ, Jing Q, et al. Tearing, folding and deformation of a carbon-carbon sp(2)-bonded network. Carbon. 2006;44(8):1544-7.
[137] Meyer JC, Geim AK, Katsnelson MI, Novoselov KS, Booth TJ, Roth S. The structure of suspended graphene sheets. Nature. 2007;446(7131):60-3.
[138] Meyer JC, Geim AK, Katsnelson MI, Novoselov KS, Obergfell D, Roth S, et al. On the roughness of single- and bi-layer graphene membranes. Solid State Commun. 2007;143(1-2):101-9.

[139] Ferrari AC, Meyer JC, Scardaci V, Casiraghi C, Lazzeri M, Mauri F, et al. Raman spectrum of graphene and graphene layers. Phys Rev Lett. 2006;97(18):-.
[140] Ferrari AC. Raman spectroscopy of graphene and graphite: Disorder, electron-phonon coupling, doping and nonadiabatic effects. Solid State Commun. 2007;143(1-2):47-57.
[141] Dresselhaus MS, Dresselhaus G, Jorio A, Souza AG, Pimenta MA, Saito R. Single nanotube Raman spectroscopy. Accounts Chem Res. 2002;35(12):1070-8.
[142] Becerril HA, Mao J, Liu Z, Stoltenberg RM, Bao Z, Chen Y. Evaluation of solution-processed reduced graphene oxide films as transparent conductors. ACS Nano. 2008;2(3):463-70.
[143] Wang X, Zhi LJ, Tsao N, Tomovic Z, Li JL, Mullen K. Transparent carbon films as electrodes in organic solar cells. Angewandte Chemie-International Edition. 2008;47(16):2990-2.
[144] Chen YC, Yu CY, Fan YL, Hung LI, Chen CP, Ting C. Low-bandgap conjugated polymer for high efficient photovoltaic applications. Chem Commun. 2010;46(35):6503-5.
[145] Tak YH, Kim KB, Park HG, Lee KH, Lee JR. Criteria for ITO (indium-tin-oxide) an organic light thin film as the bottom electrode of emitting diode. Thin Solid Films. 2002;411(1):12-6.
[146] Irwin MD, Buchholz B, Hains AW, Chang RPH, Marks TJ. p-Type semiconducting nickel oxide as an efficiency-enhancing anode interfacial layer in polymer bulk-heterojunction solar cells. P Natl Acad Sci USA. 2008;105(8):2783-7.
[147] Sierros KA, Kukureka SN. Mechanical integrity of touch-screen components. J Soc Inf Disp. 2009;17(11):947-52.
[148] The van der Pauw Technique. [cited 2010; Four contact configuration of the van der Pauw measurement technique]. Available from: http://www.nist.gov/pml/div683/hall_effect.cfm
[149] Webster JG. Electrical measurement, signal processing, and displays. Principles and applications in engineering series. Boca Raton: CRC Press, 2003, p. 1 v.
[150] Banaszczyk J, Schwarz A, De Mey G, Van Langenhove L. The Van der Pauw Method for Sheet Resistance Measurements of Polypyrrole-Coated Para-aramide Woven Fabrics. J Appl Polym Sci. 2010;117(5):2553-8.
[151] Graphene Structure. [cited 2010; Structure of a graphene layer]. Available from: http://www.craigbanksresearch.com/page3.html